



OPEN ACCESS

EDITED BY

Jaroslav Chum,
Institute of Atmospheric Physics (ASCR),
Czechia

REVIEWED BY

David R. Shklyar,
Space Research Institute (RAS), Russia
Zbysek Mosna,
Institute of Atmospheric Physics (ASCR),
Czechia

*CORRESPONDENCE

L. A. Da Silva,
ligia.alves01@gmail.com

SPECIALTY SECTION

This article was submitted to Space
Physics,
a section of the journal
Frontiers in Astronomy and Space
Sciences

RECEIVED 15 June 2022

ACCEPTED 17 August 2022

PUBLISHED 28 September 2022

CITATION

Da Silva LA, Shi J, Resende LCA,
Agapitov OV, Alves LR, Batista IS, Arras C,
Vieira LE, Deggeroni V, Marchezi J,
Wang C, Moro J, Inostroza A, Li H,
Medeiros C, Cardoso FR, Jauer P,
Alves MV, Chen SS, Liu Z, Denardini CM
and Gonzalez W (2022), The role of the
inner radiation belt dynamic in the
generation of auroral-type sporadic E-
layers over south American
magnetic anomaly.
Front. Astron. Space Sci. 9:970308.
doi: 10.3389/fspas.2022.970308

COPYRIGHT

© 2022 Da Silva, Shi, Resende, Agapitov,
Alves, Batista, Arras, Vieira, Deggeroni,
Marchezi, Wang, Moro, Inostroza, Li,
Medeiros, Cardoso, Jauer, Alves, Chen,
Liu, Denardini and Gonzalez. This is an
open-access article distributed under
the terms of the [Creative Commons
Attribution License \(CC BY\)](https://creativecommons.org/licenses/by/4.0/). The use,
distribution or reproduction in other
forums is permitted, provided the
original author(s) and the copyright
owner(s) are credited and that the
original publication in this journal is
cited, in accordance with accepted
academic practice. No use, distribution
or reproduction is permitted which does
not comply with these terms.

The role of the inner radiation belt dynamic in the generation of auroral-type sporadic E-layers over south American magnetic anomaly

L. A. Da Silva^{1,2*}, J. Shi¹, L. C. A. Resende^{1,2}, O. V. Agapitov³,
L. R. Alves², I. S. Batista², C. Arras⁴, L. E. Vieira², V. Deggeroni²,
J. P. Marchezi^{1,2}, C. Wang¹, J. Moro^{1,2}, A. Inostroza², H. Li¹,
C. Medeiros², F. R. Cardoso⁵, P. Jauer^{1,2}, M. V. Alves², S. S. Chen²,
Z. Liu¹, C. M. Denardini² and W. Gonzalez^{1,2}

¹State Key Laboratory of Space Weather, National Space Science Center, Chinese Academy of Sciences, Beijing, China, ²National Institute for Space Research—INPE, São José dos Campos, Brazil, ³University of California, Berkeley—UCB—Space Sciences Laboratory, Berkeley, CA, United States, ⁴German Research Centre for Geosciences—GFZ, Potsdam, Germany, ⁵University of São Paulo—USP, Lorena School of Engineering (EEL), São Paulo, Brazil

The dynamics of the electron population in the Earth's radiation belts affect the upper atmosphere's ionization level through the low-energy Electron Precipitation (EP). The impact of low-energy EP on the high-latitude ionosphere has been well explained since the 1960's decade. Conversely, it is still not well understood for the region of the South American Magnetic Anomaly (SAMA). In this study, we present the results of analysis of the strong geomagnetic storm associated with the Interplanetary Coronal Mass Ejection (May 27–28, 2017). The atypical auroral sporadic E layers (E_s) over SAMA are observed in concomitance with the hiss and magnetosonic wave activities in the inner radiation belt. The wave-particle interaction effects have been estimated, and the dynamic mechanisms that caused the low-energy EP over SAMA were investigated. We suggested that the enhancement in pitch angle scattering driven by hiss waves result in the low-energy EP (≥ 10 keV) into the atmosphere over SAMA. The impact of these precipitations on the ionization rate at the altitude range from 100 to 120 km can generate the E_s layer in this peculiar region. In contrast, we suggested that the low-energy EP (≤ 1 keV) causes the maximum ionization rate close to 150 km altitude, contributing to the E_s layer occurrence in these altitudes.

KEYWORDS

inner radiation belt, auroral-type sporadic E-layers, South American Magnetic Anomaly, hiss waves, magnetosonic waves, wave-particle interaction, ionosphere

Key points

- Pitch angle scattering driven by hiss waves could cause the electron precipitation ≥ 0.5 keV over the SAMA.
- Electron precipitation ≤ 10 keV is the main ingredient to generate E_{s_a} layer detected close to 100-120 km over SAMA.
- Electron precipitation ≤ 1 keV is the main ingredient to generate E_{s_a} layer detected close to 150 km over SAMA.

Introduction

Coupling between the solar wind structures and the Earth's magnetosphere can affect the upper atmosphere's ionization through charged particle precipitation. The high-latitude dynamic after the low-energy Electron Precipitation (EP) has been well understood since the 1960's decade. Rees (1963) and Cai and Ma (2007) found that the low-energy EP (≥ 1 keV) can cause maximum ionization at altitudes below 150 km. These charged particles can be an essential source to generate the auroral-type sporadic E layer (E_{s_a}) at high latitudes (Whitehead, 1970). Nath et al. (1980) suggested that low-energy EP is usually the major cause for the generation of such a layer, once the modified wind shear mechanism is important under low-energy EP conditions only.

The E_{s_a} layer over the South American Magnetic Anomaly (SAMA) has been observed since the 1970's, in which the theoretical discussions regarding the inner radiation belt dynamic were suggested as the main mechanisms responsible for the low-energy EP over this region (Batista and Abdu, 1977). SAMA is a weak magnetic field region that results from the geomagnetic field's geometric configuration (Pinto and Gonzalez, 1989) and has pronounced departures in its symmetry. This peculiar region presents the trapped particle mirror points considerably lowered in altitude compared to other areas around the Earth (Roederer, 1967).

The dynamic mechanisms in the inner radiation belt are crucial to understanding the mechanisms responsible for the low-energy EP over the SAMA (Paulikas, 1975; Batista and Abdu, 1977; Pinto and Gonzalez, 1989; Nishino et al., 2006). Therefore, observing the magnetospheric wave activities inside the inner radiation belt and slot region allows us to understand the physical processes that cause these atypical layers over the SAMA, as Gonzalez et al. (1987) suggested. In this context, the plasma waves can be detected, such as the hiss (Meredith et al., 2004) and magnetosonic (Boardsen et al., 2016) waves. The plasmaspheric hiss waves are regarded as Extremely Low Frequency (ELF) whistler-mode emission (20 Hz - few kHz) (Meredith et al., 2004; Cao et al., 2005). The fast magnetosonic (MS) waves are typically detected between the proton gyrofrequency (f_{cp}) and the lower hybrid resonance frequency ($fLHR$) (e.g., Russell et al., 1969; Ma et al., 2013).

The lightning-generated whistlers could also play an important role in electron precipitation from the Earth's inner radiation belt and slot region (see, e.g., Inan et al., 1989; Green et al., 2005; Green et al., 2020). Generally, the lightning-generated wave power could be mixed into the high frequency (> 2 kHz) portion of plasmaspheric hiss in the observation (Meredith et al., 2007). However, they are distinguishable using the wave polarization properties observations and could affect the electrons at lower energies than hiss (Green et al., 2020).

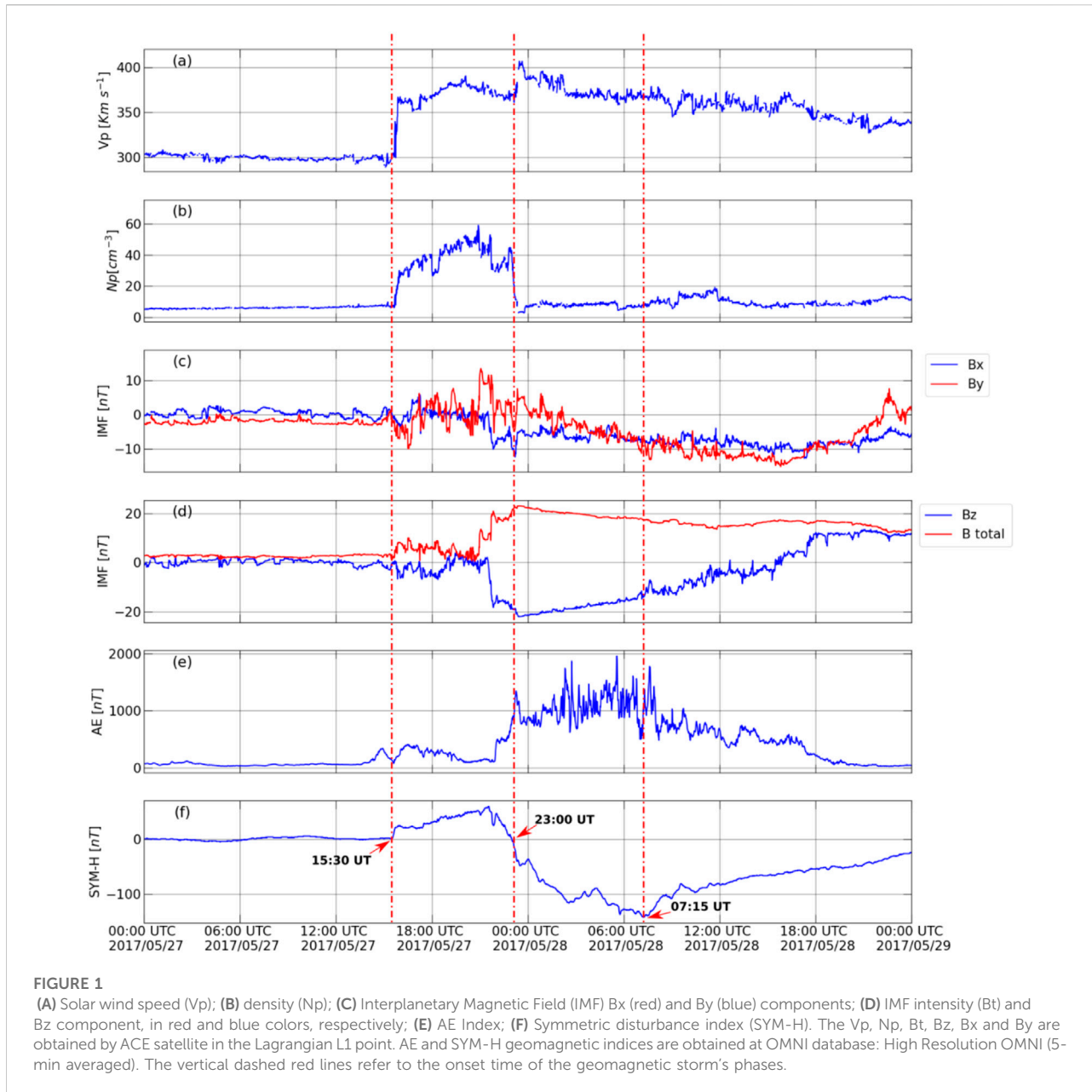
The pitch angle scattering is the main dynamic mechanism responsible for the EP driven by hiss waves (Lyons et al., 1972; Abel and Thorne 1998). On the other hand, the MS wave-particle interaction can result in EP in the atmosphere through the bounce resonance mechanism (Chen et al., 2015; Maldonado et al., 2016; Maldonado and Chen, 2018), Landau resonance mechanism (Li et al., 2014; Bortnik et al., 2015; Ma et al., 2016), and transit-time scattering mechanism (Bortnik and Thorne, 2010; Lei et al., 2017).

This work proposes to study the inner radiation belt/slot dynamic during the low-energy EP into the ionized atmosphere. The confirmation of the low-energy EP occurrence is through the E_{s_a} layer's signatures in two digital ionosondes installed close to the SAMA region. Then, the main physical processes responsible for this E_{s_a} layers' generation over SAMA are determined for the first time, using *in situ* satellite measurements in the inner radiation belt and an empirical model of the atmospheric ionization. Finally, the dynamic mechanisms responsible for the extra atmosphere's ionization over the SAMA region are identified, leading to a better understanding of the magnetosphere-ionosphere coupling, and answering many open questions, as follows below:

1. Why the auroral-type sporadic E layer is detected over the SAMA region (outside the auroral region)?
2. What are the magnetosphere waves and the main dynamic mechanism that cause the electron precipitation over the SAMA region?
3. What energy levels of electrons precipitate over the SAMA region?
4. What energy levels of electrons can generate the E_{s_a} layers close to 100-120 km over SAMA?
5. What energy levels of electrons can generate the E_{s_a} layers close to 150 km over SAMA?

Approach

We aim to investigate the low-energy EP (tens of keV) in the ionosphere over the SAMA. For this purpose, we use space and ground-based observations recorded over several decades. However, we have constraints on how we can proceed in this investigation. For example, we need simultaneous observations



of the solar wind, the magnetosphere, and ionospheric conditions. Additionally, it would be simpler to investigate periods in which the low-energy EP effects would be easily distinguishable from the background patterns. In this work, we select an event to study the signatures in the inner radiation belt that are associated with the ionosphere.

Assuming that low-energy EP occurs during geomagnetic storm conditions, it is reasonable in the first moment to search for signatures in the ionosphere during intense geomagnetic storms. As defined by Gonzalez et al. (1994), intense geomagnetic storms are usually related to the transit of interplanetary counterparts of coronal mass ejections (ICMEs)

through Earth's orbit. In this way, we identify the candidate events in the ICME events catalog compiled by Cane & Richardson (2003) and Richardson & Cane (2010). Currently, the event list is available at <http://www.srl.caltech.edu/ACE/ASC/DATA/level3/icmetable2.htm>.

This work investigates the solar wind structure employing parameters measured by instruments onboard the Advanced Composition Explorer (ACE) satellite, which provided the solar wind parameters at the L1 Lagrangian point since 1997 (Stone et al., 1998). Specifically, we use observations from the Magnetic Field Experiment (MAG) and Solar Wind Electron, Proton, and Alpha Monitor (SWEPAM).

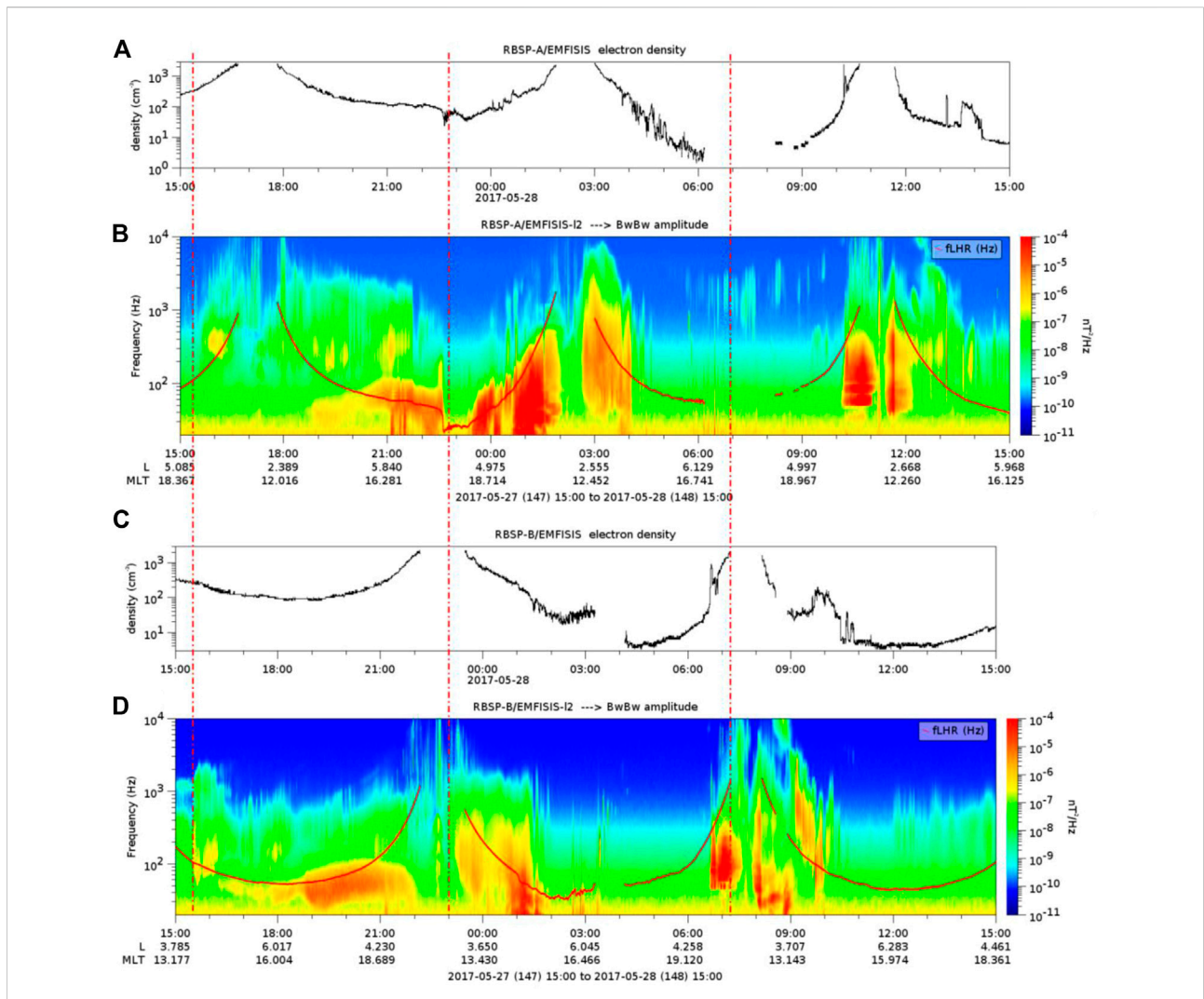
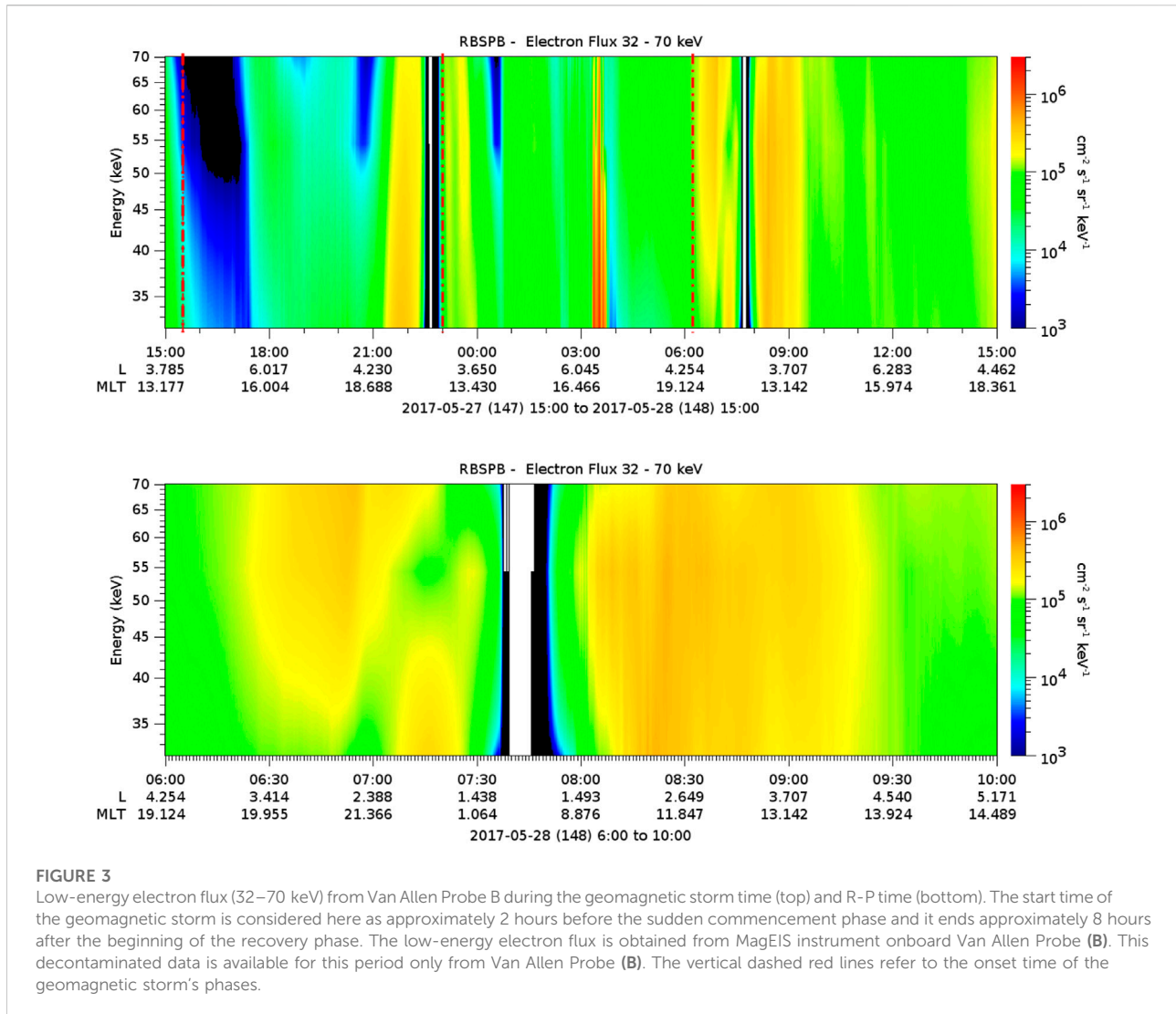


FIGURE 2
 Electron density from Van Allen Probe A (A) and B (C), and frequency-time spectrogram of magnetic spectral density from Van Allen Probe A (B) and B (D). The red line represents the lower hybrid resonance frequency (*fLHR*). The electron densities and *fLHR* are obtained from the EMFISIS instrument. The geomagnetic storm period analyzed here is approximately 2 hours before the sudden commencement phase and about 8 hours after the beginning of the recovery phase. The vertical dashed red lines refer to the onset time of the geomagnetic storm's phases.

On the other hand, we need to identify a signature of the low-energy EP in the ionosphere appropriate for this study. The E_s layer is a suitable signature for such investigation as low-energy EP is associated with these sporadic E layers in the auroral region. Here, we use the data collected by Digisondes installed in Cachoeira Paulista, Brazil (22.7°S, 45.0°W, dip: -35°, L = 1.13), from the Embrace Network (Denardini et al., 2016), and installed in Santa Maria, Brazil (29.7°S, 53.8°W, dip: -37°, L = 1.16) from the China-Brazil Joint Laboratory for Space Weather (Moro et al., 2019) to monitor the occurrence of E_s layer over the SAMA region. The ionograms are graphs of virtual height versus frequency, which provide the ionospheric profile, and from which the ionospheric parameters, including the sporadic-E layer types, can be obtained. These graphs are obtained from

the ionosondes, a radar that transmits radio waves continuously into the ionosphere ranging from 1 to 30 MHz and 5/10 min of time resolution (Reinisch et al., 2009). It is important to mention that virtual heights are calculated based on the time interval between pulse transmission and echo received through the antennas (Reinisch et al., 1997).

The Van Allen Probes Mission (VAP), which was designed to investigate the dynamics of the Earth's radiation belts, has been providing observations of low-energy electron flux and the wave activity for approximately 7 years since its launch on 12 August 2012 (Mauk et al., 2013). The proton flux contamination in the Magnetic Electron Ion Spectrometer (MagEIS - Blake et al., 2013) data of the Van Allen Probes has been removed (Claudepierre et al., 2015), providing the low-energy electrons trapped without contamination.



In contrast, the low-energy electrons precipitated over SAMA are still challenging to measure due to the strong proton contamination (e.g., Rodger et al., 2013; Andersson et al., 2014). In this way, we analyze and discuss the low-energy electrons in the inner radiation belt/slot as well as the plasma waves. The plasma waves, such as hiss waves (Meredith et al., 2004), can interact with these electrons through the pitch angle scattering mechanism to cause EP to the atmosphere. In contrast, the MS waves (Ma et al., 2013) can interact with these electrons through bounce resonance, Landau resonance, or transit-time scattering mechanisms to cause EP to the atmosphere. Furthermore, an empirical model (Fang et al., 2010) is used to estimate the atmospheric ionization rate (100–150 km) and confirm the role of the low-energy EP in the E_s layer generation over this peculiar region.

The hiss and MS wave power spectral densities are estimated using observations from the Electric and Magnetic Field

Instrument Suite and Integrated Science (EMFISIS) instrument (Kletzing et al., 2013). We infer the total electron density from the data measured by the Electric Field and Waves (EFW) instrument (Wygant et al., 2013) and the frequency ratio of electron plasma oscillation to electron cyclotron gyration (f_{pe}/f_{ce}) from the EMFISIS instrument. We compute the Wave Normal Angle (WNA), ellipticity, and planarity based on the singular value decomposition method (Santolík et al., 2003). For this, we use data from the waveform receiver (WFR) integrated into EMFISIS.

Based on these constraints, we selected one ICME event observed on May 27–28, 2017, which is concomitant to an intense geomagnetic storm and the occurrence of the E_s layer over SAMA. For these analyses, we consider that the geomagnetic storm evolves in different phases related to the structure of the ICME.

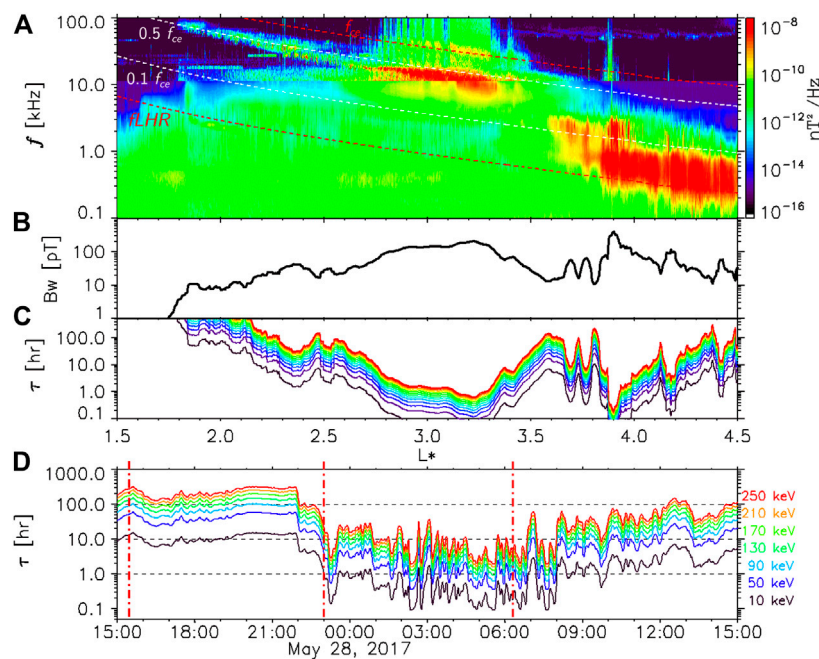


FIGURE 4

(A) Dynamic spectrum of chorus wave magnetic field from Van Allen Probe B, obtained from EMFISIS on 2017-05-28 (08:00-09:30UT) below 10 kHz and HFR (electric field was recalculated into magnetic field magnitude under the approximation of field aligned propagation) above 10 kHz. (B) Chorus waves amplitude, B_w (pT). (C) Time scale for electron (10-1,000 keV) quasi-linear scattering by lower band chorus waves, $\tau = 1/D_{aa}$. (D) The 10-250 keV electron lifetime (τ) dynamics at $L^* = 2.5$ during the time interval from Figure 2 (electron energies are color coded). Electron cyclotron frequency f_{ce} and lower hybrid frequency f_{LHR} are indicated by the red curves, $0.5 f_{ce}$ and $0.1 f_{ce}$ are indicated by the white curves. The vertical dashed red lines refer to the onset time of the geomagnetic storm's phases.

Interplanetary medium conditions and geomagnetic storm

The scenery of this study occurred under the influence of an ICME, which can drive a geomagnetic storm (Gonzalez et al., 1999; Echer et al., 2008; Richardson and Cane, 2012), and deposit energy in the magnetosphere (Ponomarev et al., 2006). An ICME reached the L1 Lagrangian point at 15:30 UT on 27 May 2017, in which the solar wind speed (Figure 1A) and the proton density (Figure 1B) abruptly increased, from ~ 290 to 365 km/s and from ~ 7 to 30 proton/cm³, respectively. These abrupt increases occurred concomitantly with the signature of the storm's sudden commencement (SC-P) (first vertical dashed red line) observed in the SYM-H (Figure 1F). This SC-P (SYM-H positive) persists until $\sim 23:00$ UT on May 27, and the maximum positive value is $\sim +60$ nT. By component (Figure 1C red line) fluctuates between -10 nT and $+12$ nT during the SC-P. The B_z component (Figure 1D blue line) is southward oriented, and the AE index (Figure 1E) oscillates below 500 nT, except at $\sim 23:00$ UT when it reached ~ 500 nT.

The storm's main phase (M-P) started at $\sim 23:00$ UT on May 27 (the second vertical dashed red line), in which the SYM-H (Figure 1F) values crossed zero, and it persisted decreasing until

07:15 UT on May 28. During this M-P, the proton density (Figure 1B) decreases significantly (<10 proton/cm⁻³), B_z component (Figure 1D red line) reached ~ -20 nT, and the AE index (Figure 1E) reached a maximum value of approximately 1,600 nT at $\sim 02:00$ UT and $05:30$ UT on May 28, persisting above $\sim 1,000$ nT on average. The storm's recovery phase (R-P) started at $\sim 07:15$ UT on May 28 (the third vertical dashed red line), in which the SYM-H (Figure 1F) began to increase. The AE index (Figure 1E) reached ~ 1700 nT at $\sim 07:30$ UT on May 28.

Inner radiation belt dynamic and low-energy EP over SAMA

The energy deposited in the inner magnetosphere, under the influence of this ICME, is considerably strong (Ponomarev et al., 2006). This energy can generate magnetospheric waves in a wide range of frequencies (e.g., Da Silva et al., 2021), especially during the geomagnetic storm's phases. The magnetospheric waves can interact with the electron and can cause particle precipitation to the atmosphere. The electron particle precipitation can be observed over both the auroral and SAMA regions. Precisely,

TABLE 1 The Magnetic Local Time (MLT) and L values of the VAP-A/B and the ionosonde stations during the conjunctions. The conjunctions were observed only during the storm's main and recovery phases.

Storm's main phase (M-P)			
05/28/2017	Van Allen Probe A	Cachoeira Paulista	Santa Maria
1:36 UT	MLT = 21.86, L = 2.48	MLT = 22.38, L = 1.13	MLT = 21.78, L = 1.16
1:44 UT	MLT = 22.51, L = 2.17	MLT = 22.51, L = 1.13	MLT = 21.90, L = 1.16
Storm's recovery phase (R-P)			
05/28/2017	Van Allen Probe B	Cachoeira Paulista	Santa Maria
7:40 UT	MLT = 3.75, L > 1.17	MLT = 4.31, L = 1.13	MLT = 3.71, L = 1.16
7:42 UT	MLT = 4.37, L > 1.17	MLT = 4.35, L = 1.13	MLT = 3.75, L = 1.16
Storm's recovery phase (R-P)			
05/28/2017	Van Allen Probe A	Cachoeira Paulista	Santa Maria
11:21 UT	MLT = 7.36, L = 1.32	MLT = 8.01, L = 1.13	MLT = 7.41, L = 1.16
11:24 UT	MLT = 8.08, L = 1.34	MLT = 8.05, L = 1.13	MLT = 7.46, L = 1.16

over the SAMA region, the low-energy EP (tens to hundreds keV) arising from the inner radiation belt can be estimated through the measurements of the X-rays emission, as observed by [Pinto and Gonzalez \(1989\)](#); [Pinto et al. \(1989\)](#) and [Kuznetsov, \(2007\)](#).

Due to trapped particle mirror points being considerably lowered in altitude as they drift through the SAMA ([Roederer, 1967](#)), this region is significantly contaminated by the protons. It implies the difficulty of measuring the electron flux in the inner radiation belt and the electron precipitation (e.g., [Rodger et al., 2013](#); [Andersson et al., 2014](#)). However, the background contamination of the electron flux measurements from MagEIS was removed ([Claudepierre et al., 2015](#)) and is used here to discuss the low-energy electron flux variability in the inner radiation belt and their possible relationship with the plasma waves. Consequently, the main physical processes responsible for launching the electron particles in the loss cone over this region are identified.

Plasma wave activities and low-energy electron flux variability during the geomagnetic storm's phases

The plasma waves, such as the plasmaspheric hiss and magnetosonic waves can be detected in the inner radiation belt. This region can be coincident with the plasmasphere region and will be identified by the total electron density. The

total electron density is a fundamental parameter of plasma; here specifically, it is used to map regions of the magnetosphere, such as the plasmasphere. This parameter is estimated through the higher-frequency measurements obtained from the EMFISIS instrument onboard Van Allen Probes, which is able to measure a single electric field component of waves in the frequency range of 10–500 kHz. These higher-frequency measurements allow the determination of the total electron density at the spacecraft, which can be inferred from the upper hybrid resonance frequency f_{UH} . The upper hybrid resonance frequency is defined as $\omega_{uh}^2 = \omega_{ce}^2 + \omega_{pe}^2$. Where $f_{pe} = \omega_{pe}/2\pi$ and $f_{ce} = q|B|/m$, in which f_{ce} is given in hertz and $|B|$ in nanotesla, measured by *in-situ* magnetometer. The total electron density is obtained by substituting the appropriate values for the electron charge and mass (e.g., [Kurth et al., 2015](#)).

The plasmaspheric hiss waves, regarded as Extremely Low Frequency (ELF) whistler-mode emission (20 Hz to a few kHz) ([Meredith et al., 2004](#); [Cao et al., 2005](#)), are commonly observed over a broad spatial region in the plasmasphere or plasmaspheric plumes. The MS waves are typically detected between the proton gyrofrequency (f_{cp}) and the f_{LHR} (e.g., [Russell et al., 1969](#); [Ma et al., 2013](#)). These waves can play an essential role in the loss process of energetic electrons in the inner magnetosphere, being able to cause electron precipitation ([Li J. et al., 2019](#); [Yahnin et al., 2019](#)). Thus, analyzing the global spatiotemporal evolution of these waves' intensities during the geomagnetic storm's phases is

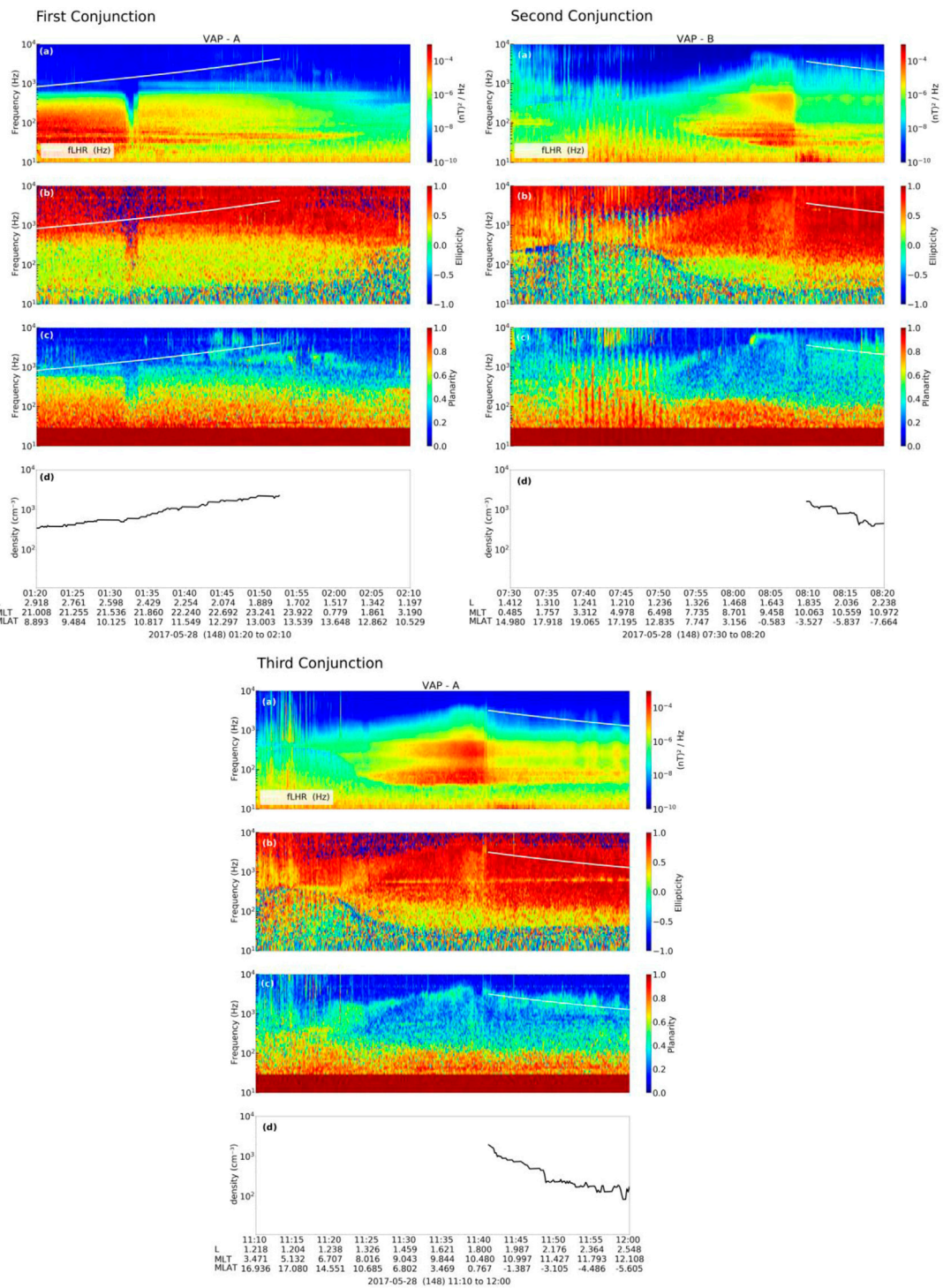


FIGURE 5

(A) The frequency-time spectrogram of the magnetic field; (B) ellipticity; (C) planarity and (D) the total electron density during the first (left panels), second (right panels) and third (bottom panels) conjunctions. The lower hybrid resonance frequency (f_{LHR}) (white line) are presented in panels (A–C). The ellipticity and planarity are calculated through the singular value decomposition method (Santolik et al., 2003). The f_{LHR} and frequency-time spectrogram of magnetic field are obtained from EMFISIS instrument and the electron density is inferred from the data of EFW instrument. The EFW and EMFISIS instruments are onboard the VAP.

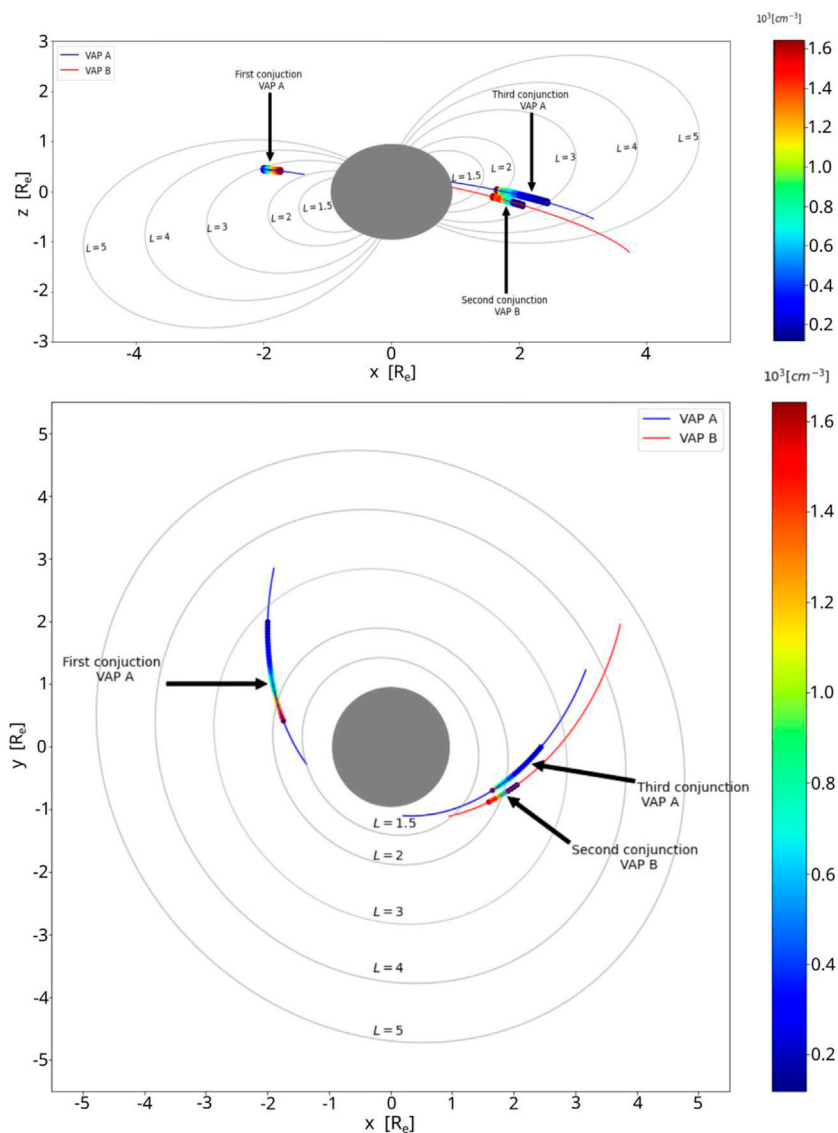


FIGURE 6

Spatial distribution in two dimensions of electron density for L values 1.5, 2, 3, 4, and 5 using a dipolar model of Earth’s magnetic field lines in the Solar Magnetic coordinate (SM) for plane YZ (top panel) and XY (bottom panel). The total electron density measurements were obtained from the EMFISIS instrument onboard the Van Allen Probes A (blue lines) and B (red lines). The color bar is the total electron density value.

important to identify the main dynamic mechanisms responsible for launching the electron particles in the loss cone, which can result in particle precipitation over SAMA. For that, we use the spectrograms of the magnetic field from the EMFISIS instrument onboard the Van Allen Probes to detect the plasma wave activities, considering the periods when the Van Allen Probes orbit was next to the perigee ($\sim L < 3.5$).

Figure 2 presents the electron densities, the spectrograms of the magnetic field and $fLHR$ obtained from the EMFISIS instrument onboard Van Allen Probes A (panels a and b) and B (panels c and d). The electron density is a fundamental

parameter of plasma obtained from plasma wave measurements made onboard Van Allen Probes (Kurth et al., 2015). In accordance with the literature, the plasmasphere is considered the innermost region of the magnetosphere. It is formed by a thermal plasma cloud encircling the Earth, in which their electron density varies between $\sim 10\text{--}10^4$ electrons/cm³. In contrast, the outside of the plasmasphere is formed by hot plasma, where the electron density changes abruptly to tenuous density (~ 1 electron/cm³). Thereby, the boundary that separates the low-density plasma region from the high-density plasma region is called

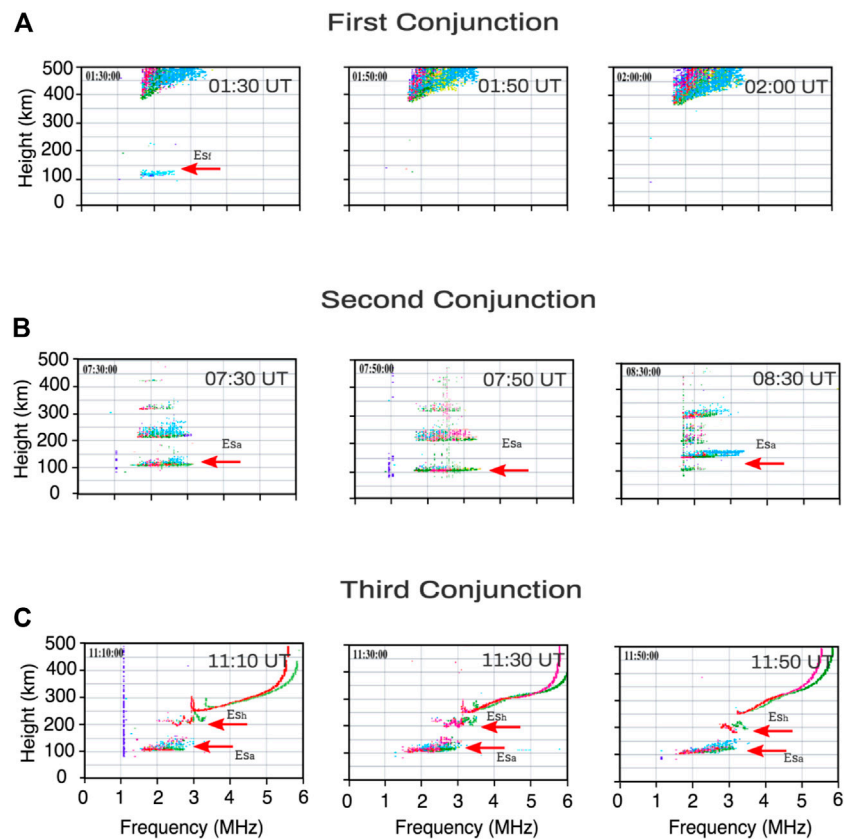


FIGURE 7

Ionograms from Digisonde located at Cachoeira Paulista station during the first (A), second (B) and third (C) conjunctions. The red arrows show the Es layers presence. The color code in these ionograms represents the echo direction of the signal received. Red shades denote O-polarization, and green shades indicate X-polarization. The blue points are used for the echoes in the North/East directions, and yellow shades are used for the South/West. More details can be found at <https://giro.uml.edu/ionogram-data.html>.

plasmopause, which is represented by the variation of the ratio between the maximum and minimum electron density, as widely used in previous studies (e.g., Guo et al., 2021; Thomas et al., 2021; Zhelavskaya et al., 2016; Liu et al., 2015; Lemaire et al., 1998). The determination of the plasmopause allows the identification of the plasmaspheric waves. On the other hand, the *fLHR* identifies the MS wave activities. The time duration of Figure 2 (15:00 UT on May 27 to 15:00 UT on May 28) includes the storm's sudden commencement, main, and recovery phase.

The Van Allen probe A (RBSP-A) presented three periods at the perigee, while the Van Allen probe B (RBSP-B) presented two periods:

The RBSP-A periods:

- 1) The first period (15:00UT - 19:00UT on May 27) refers to the storm's sudden commencement phase (SC-P).
- 2) The second period (00:00UT - 04:00UT on May 28) is referent to the storm's main phase (M-P).

- 3) The third period (09:00UT - 13:00UT on May 28) is referent to the storm's recovery phase (R-P).

The RBSP-B periods:

- 1) The first period (21:00UT on May 27 and 01:00UT on May 28) occurred during the storm's sudden commencement phase and storm's main phase (SC-M-P);
- 2) The second period (06:00UT - 10:00UT on May 28) occurred during the storm's recovery phase (R-P).

The spectrogram of the magnetic field observed in Figure 2 (panel b - RBSP-A) during the SC-P suggests the presence of the plasmaspheric hiss waves at ~ 16:00 UT and from 18:00 UT below the plasmopause (panel a). The spectrogram also shows the discrete MS waves around 19:00 UT, observed below *fLHR*. During the M-P (panel b - RBSP-A), the power spectral density suggests the presence of the plasmaspheric wave activities during all-time analyzed (00:00UT - 04:00UT on

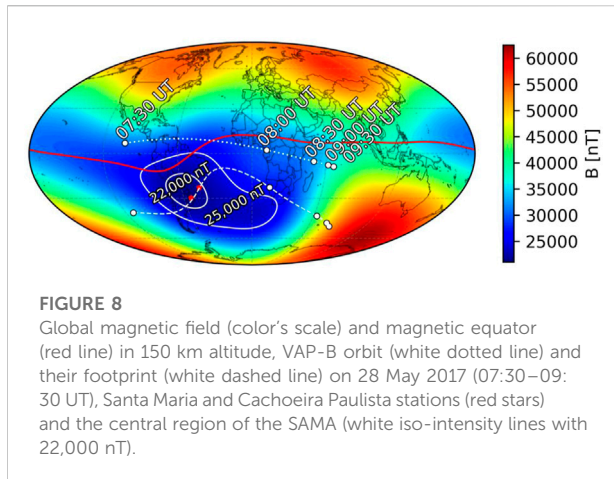


FIGURE 8
Global magnetic field (color's scale) and magnetic equator (red line) in 150 km altitude, VAP-B orbit (white dotted line) and their footprint (white dashed line) on 28 May 2017 (07:30–09:30 UT), Santa Maria and Cachoeira Paulista stations (red stars) and the central region of the SAMA (white iso-intensity lines with 22,000 nT).

May 28), in which the power spectral is considerably strong compared with the SC-P period, and below $fLHR$. During the R-P (panel b - RBSP-A), the plasma wave activities are observed again, below the plasmasphere (panel a) and the $fLHR$ during all-time analyzed (09:00UT - 13:00UT on May 28). The plasmopause is apparently compressed during the R-P (panel a - RBSP-A) compared with the SC-P and M-P periods. This result was already expected due to the plasmopause being located closer to the Earth when it is under the influence of high geomagnetic activity (see Chappell et al., 1970; Goldstein, 2006; Pierrard et al., 2008).

The spectrogram of the magnetic field observed in Figure 2 (panel d - RBSP-B) during the SC-M-P suggests the signatures of the plasmaspheric wave activities within the inner radiation belt. These plasmaspheric wave activities are observed during SC-P confined below 200 Hz, while during the M-P, these waves are observed below 700 Hz. During the R-P, the behavior of the plasmasphere is similar to the period measured by the RBSP-A (09:00UT - 13:00UT on May 28), in which the plasmopause is apparently compressed (panel c) compared with the SC-M-P period.

The low-energy electron flux (32–70 keV) within the radiation belts (Figure 3) is presented here, with more detail during the R-P (bottom panel), in which the plasmopause is apparently compressed compared with the SC-M-P period (top panel). The seed population increased considerably during the R-P, compared with the SC-M-P. Before 06:50 UT, an electron flux increase is observed above 38 keV. In contrast, two electron flux decreases are observed, the first is close to 7:00 UT reaching the electrons below 45 keV, and the second is observed close to 7:15 UT reaching the electrons above 45 keV. After the perigee time (after 8:00 UT), the electron flux increase is persistent for more than 1 h and 30 min in all the range of energy presented. The plasmopause approached the Earth ($L \approx 1.8$) during the R-P, as observed in Figure 2D after 06:00 UT on May 28 (black line) and in Figure 4A at the beginning of the chorus wave activities.

This strong geomagnetic activity may produce a favorable plasma regime, as observed through the measurements of the seed population (tens keV, Figure 3) after the initial geomagnetic storm phase, which may contribute to the rapid scattering of electrons (Meredith et al., 2004; Ma et al., 2016b; Agapitov et al., 2019). Therefore, it is crucial to investigate the plasma waves and seed particles' lifetime during this period.

Figure 4 shows the chorus wave activities at extremely low L^* in usual chorus frequency bands $0.1-0.45 f_{ce}$ and $0.55-0.9 f_{ce}$ that reach up to 80 kHz. The dynamic spectrum of chorus wave magnetic field is calculated combining from EFI and HFR Van Allen Probe B measurements during geomagnetic storm R-P on 28 May 2017. Figure 4 shows that the lower band chorus waves had maximum time-averaged amplitudes of $\sim 100-140$ pT (while the statistical model from Agapitov et al., 2018, gives ~ 90 pT) at $L^* = 3$, where the f_{pe}/f_{ce} ratio was ~ 2 at $\sim 8:30$ UT (Figure not shown).

The dynamics of electron lifetime can be estimated based on the chorus model (Agapitov et al., 2015, 2018), which was extended, taking into account the cold plasma dynamics and the latitudinal distribution of wave amplitude. The results are shown in Figure 4, in which the parameters correspond to a typical quasi-linear scattering time scale $1/D_{aa}$ (30 keV) $\sim 0.4 \pm 0.1$ h at $L^* = 3$ (versus $\sim 6 \pm 0.2$ h using the statistical model from (Agapitov et al., 2019)) and ~ 2 h at $L^* = 2.3$ presumably causing intensive precipitations of 10–30 keV electrons to the ionosphere.

The dynamics of electron lifetime can be based on the hiss model (Agapitov et al., 2020), in which this new model version considers the low-energy electron levels (10–250 keV) and the latitudinal distribution from $L^* = 2.5$. Thereby, the f_{pe}/f_{ce} is considerably low (~ 2), as expected (e.g., Albert et al., 2016; Watt et al., 2019). The main results are presented in Figure 4, in which the 10–250 keV electron lifetime (τ) dynamics at $L^* = 2.5$ driven by plasmaspheric hiss waves are shown during the time interval from Figure 2. The electron energies are color coded. The quasi-linear scattering time scale $1/D_{aa}$ (10 keV) is below 1 h from 23:00 UT on May 27 to 10:00 UT on May 28, coinciding with the M-P and R-P geomagnetic storm. It means that the plasmaspheric hiss waves confined at $L^* = 2.5$ presumably cause intensive precipitations of 10 keV electrons to the ionosphere.

Plasma wave activities during the conjunctions between the Van Allen Probes and the ionosonde stations over SAMA

The plasmaspheric hiss waves have been measured at low latitude within the inner radiation belt ($L = \sim 1-2$) since the 70s decade (Tsurutani et al., 1975). These waves can trigger the dynamic mechanisms for the EP over the SAMA region, as suggested by Gonzalez et al. (1987). Therefore, planarity and

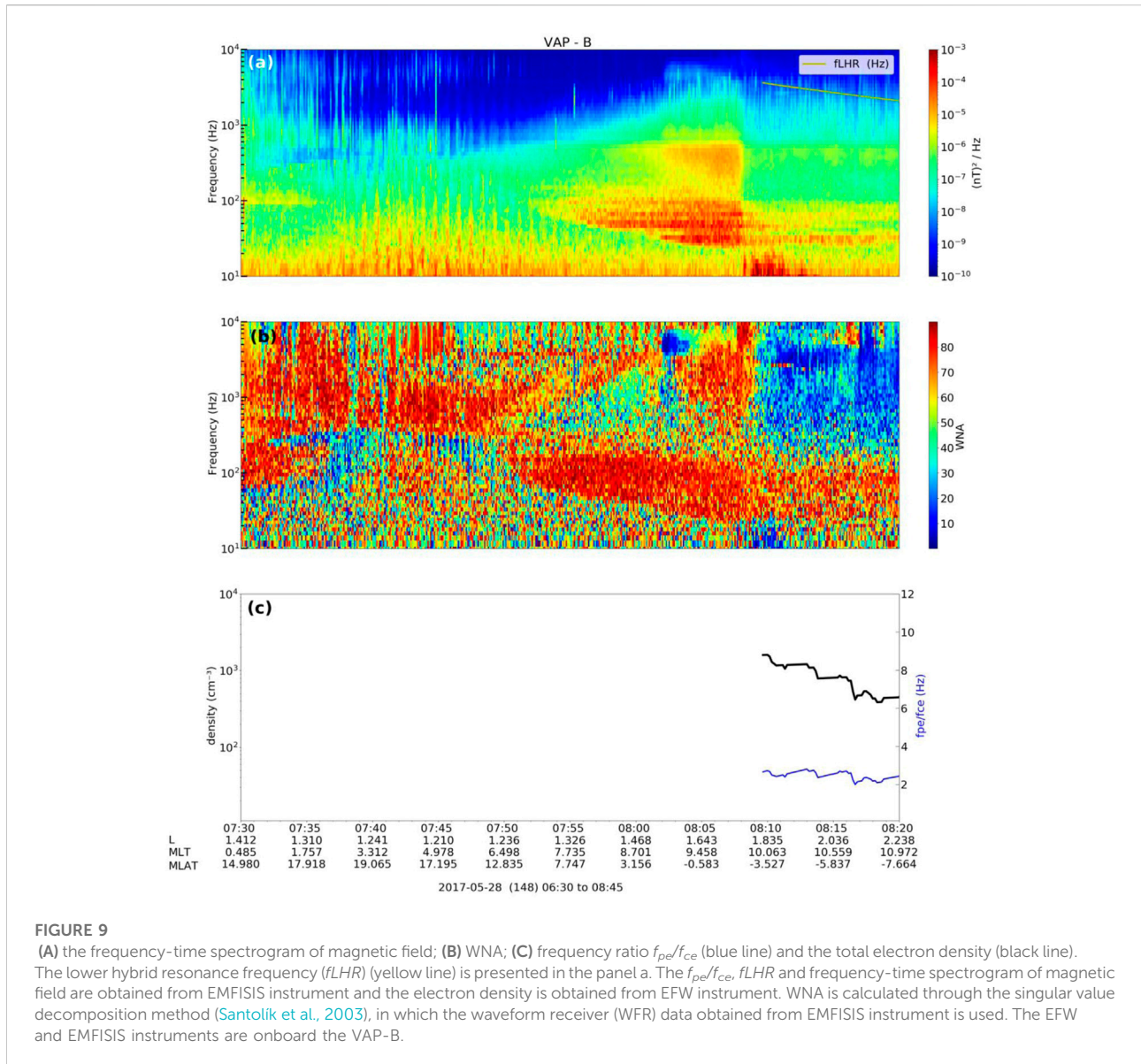


FIGURE 9 (A) the frequency-time spectrogram of magnetic field; (B) WNA; (C) frequency ratio f_{pe}/f_{ce} (blue line) and the total electron density (black line). The lower hybrid resonance frequency ($fLHR$) (yellow line) is presented in the panel a. The f_{pe}/f_{ce} , $fLHR$ and frequency-time spectrogram of magnetic field are obtained from EMFISIS instrument and the electron density is obtained from EFW instrument. WNA is calculated through the singular value decomposition method (Santolik et al., 2003), in which the waveform receiver (WFR) data obtained from EMFISIS instrument is used. The EFW and EMFISIS instruments are onboard the VAP-B.

ellipticity are used to identify the plasmaspheric waves in the inner radiation belt. Once, the planarity and ellipticity allow for classifying the degree of magnetic field polarization in the polarization plane and the ellipticity of the magnetic field polarization (Hartley et al., 2018).

The ionosonde measurements can indirectly infer the occurrences of the low-energy EP through the signature of the auroral type sporadic E layer (E_s) in this peculiar region. The ellipticity and planarity are calculated only during the conjunctions between the Van Allen Probes and the ionosonde stations over Brazil. Table 1 shows the occurrences of the three conjunctions during the entire period analyzed. The first and third conjunctions are observed between VAP-A and the ionosonde stations during the M-P and R-P, respectively. In

contrast, the conjunction between VAP-B and the ionosonde stations is observed only during the R-P.

Figure 5 presents the frequency-time spectrogram of the magnetic field (a), ellipticity (b), planarity (c) and total electron density (d) during the first (left panels), second (right panels), and third (bottom panels) conjunctions. The $fLHR$ (white line) are presented in panels (a). The plasma density and wave polarization properties are used to distinguish the different types of the plasmaspheric waves (e.g., Li et al., 2015; Li W. et al., 2019).

Figure 5 (left panels) shows the plasma waves during the first conjunction period (VAP-A, 01:20-02:10 UT), which occurs during the storm M-P. The MS wave activities are observed almost the entire time. They are detected inside the plasmasphere

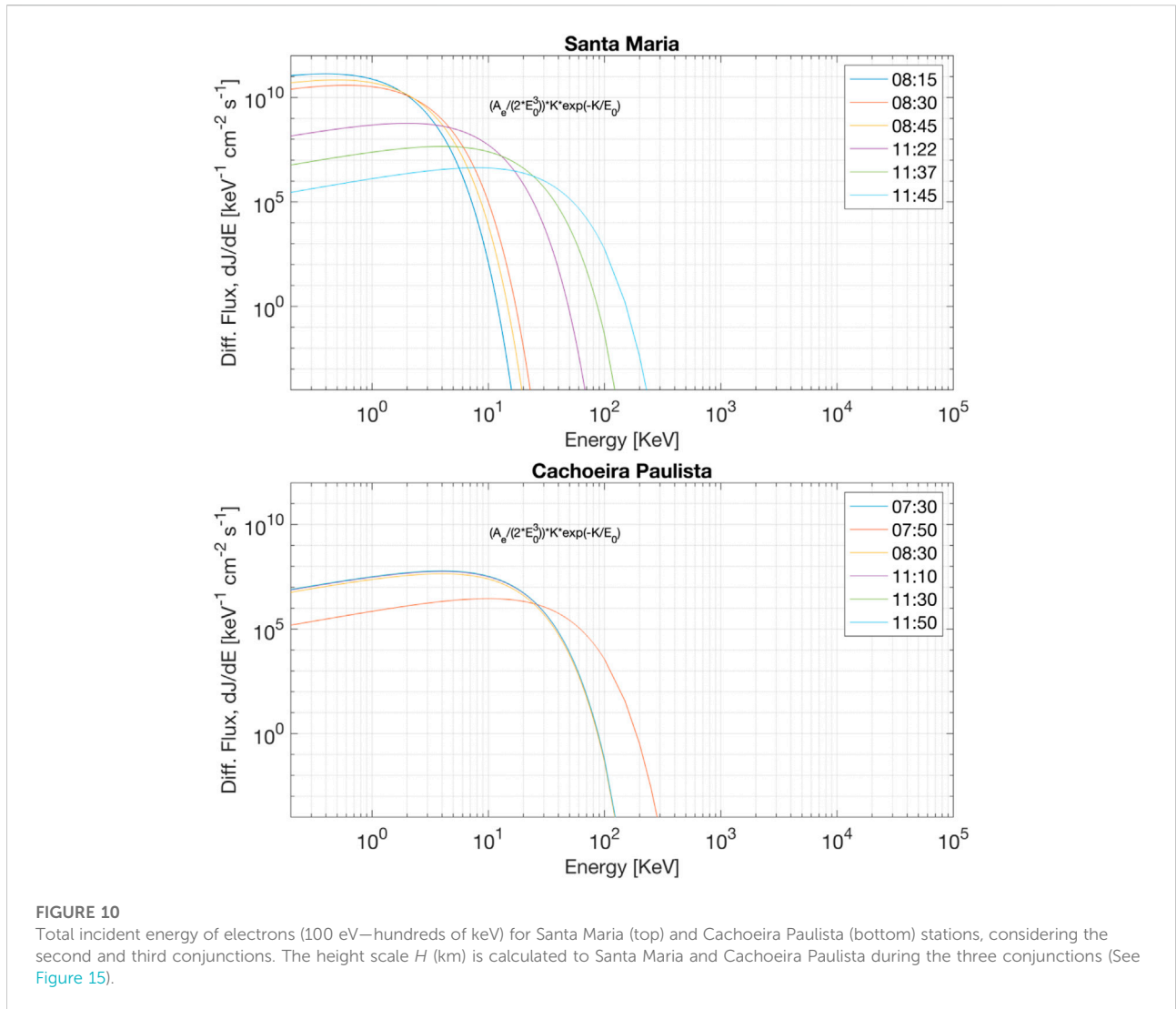


FIGURE 10 Total incident energy of electrons (100 eV–hundreds of keV) for Santa Maria (top) and Cachoeira Paulista (bottom) stations, considering the second and third conjunctions. The height scale H (km) is calculated to Santa Maria and Cachoeira Paulista during the three conjunctions (See Figure 15).

and below $fLHR$ (e.g., Laakso et al., 1990; Santolík et al., 2002). Their ellipticity is ~ 0.2 and planarity ≥ 0.8 . It means that their propagation is highly oblique related to ambient magnetic field direction and linearly polarized (e.g., Horne et al., 2007; Ma et al., 2016). Figure 5 (right panels) shows the plasma waves during the second conjunction period (VAP-B, 07:30–08:20 UT), which occurs during the storm R-P. The hiss waves are observed approximately before 07:38 UT and from 07:46 UT, with ellipticity ≥ 0.5 and planarity ≥ 0.2 (e.g., Li et al., 2015). The MS waves are detected from 07:53 UT, and their polarization ellipticity is concentrated between ± 0.2 and planarity ≥ 0.8 . Figure 5 (bottom panels) shows plasma waves during the third conjunction period (VAP-A, 11:10–12:00 UT), which occurs during the storm R-P again. The plasma wave activities are very similar to the waves detected during the second conjunction. The hiss waves are observed from 11:23 UT, with ellipticity ≥ 0.5 and planarity ≥ 0.2 (e.g., Li et al., 2015),

and the MS waves presented the ellipticity ~ 0.2 and planarity ≥ 0.8 .

Figure 6 (top and bottom panels) show the spatial distribution of the electron density in two dimensions for L values 1.5, 2, 3, 4, and 5 using a dipolar model of Earth’s magnetic field lines in the Solar Magnetic coordinate (SM) for plane YZ and XY , respectively. The total electron density measurements are obtained from the EMFISIS instrument onboard the Van Allen Probes A (conjunction 1 and 3) and B (conjunction 2), and the periods are limited by the availability of the EMFISIS data (See Supplementary Figure S1 –in Supporting Information).

Observe in Figure 6 (top and bottom panels) that SAMA L -shells correspond to approximately $1 \leq L \leq 2$ (inner radiation belt) and the auroral oval is located about $3 \leq L \leq 6$ (outer radiation belt). Additionally, the dynamic location of the plasmopause shows its preferential position within the inner radiation belt and slot region ($L < 3$) during these three

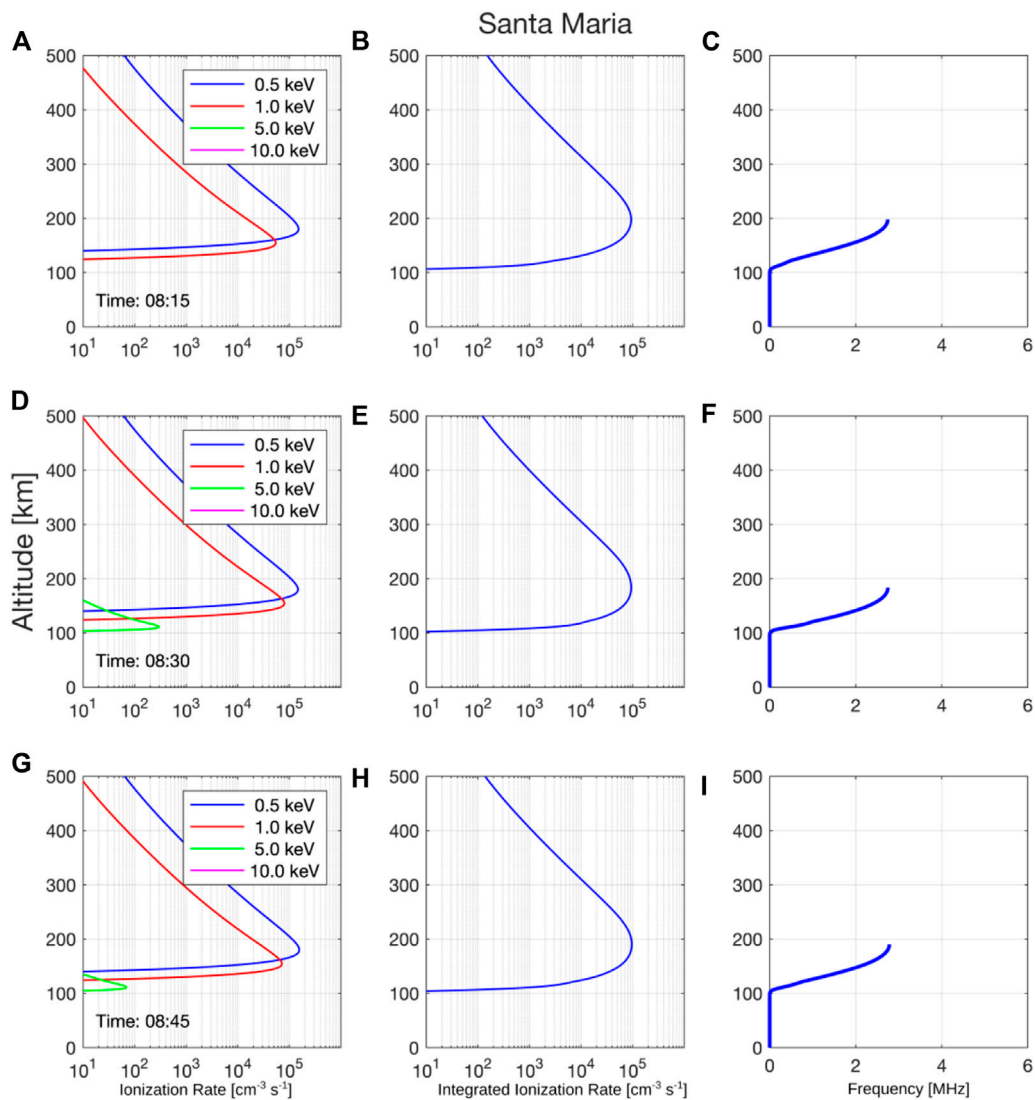


FIGURE 11 Ionization rate altitude profiles panels (A,D,G), ionization rate altitude integrated panels (B,E,H) and frequency range altitude panels (C,F,I) considering the second conjunction for Santa Maria station. The total incident energy of electrons is presented in Figure 10 (top panel). The ionization rate is obtained from empirical model (Fang et al., 2010) considering the total incident energy of electrons presented in Figure 10 (top panel) and the height scale presented in Figure 15 (top panel).

conjunctions periods. It means that the plasma waves detected within the plasmasphere are confined at $L < 3$, which may have resonantly interacted with the low-energy electrons to cause the EP to the SAMA region (lower latitude region).

The ionosonde stations used in this study are located over the SAMA region, specifically in the low-middle latitude ($20^\circ < \text{geomagnetic latitude} < 50^\circ$). Therefore, the dynamic mechanisms responsible for the Es layers generally are associated with both the vertical shear in the horizontal tidal wind (Haldoupis, 2012) and the low-energy EP (Batista and Abdu, 1977). The Es layers associated with the vertical shear in the horizontal tidal wind are normally classified into the flat (Es_f),

high (Es_h), cusp (Es_c), and low (Es_l) types, while the Es layers associated with the low-energy EP is observed in the ionograms as traces of range spreading echoes, named Es_a layer (e.g., Moro et al., 2022; Kirkwood and Nilsson, 2000; Piggott and Rawer, 1978). They are commonly detected in the auroral regions produced by the auroral particle ionization (Nikolaeva et al., 2021) from the outer radiation belt (Blum et al., 2013) and peculiarly over the SAMA region due the low-energy EP from the inner radiation belt (Batista and Abdu 1977; Gonzalez et al., 1987; Moro et al., 2022).

Figure 7 shows the ionograms over Cachoeira Paulista during the first (top panels), second (middle panels), and

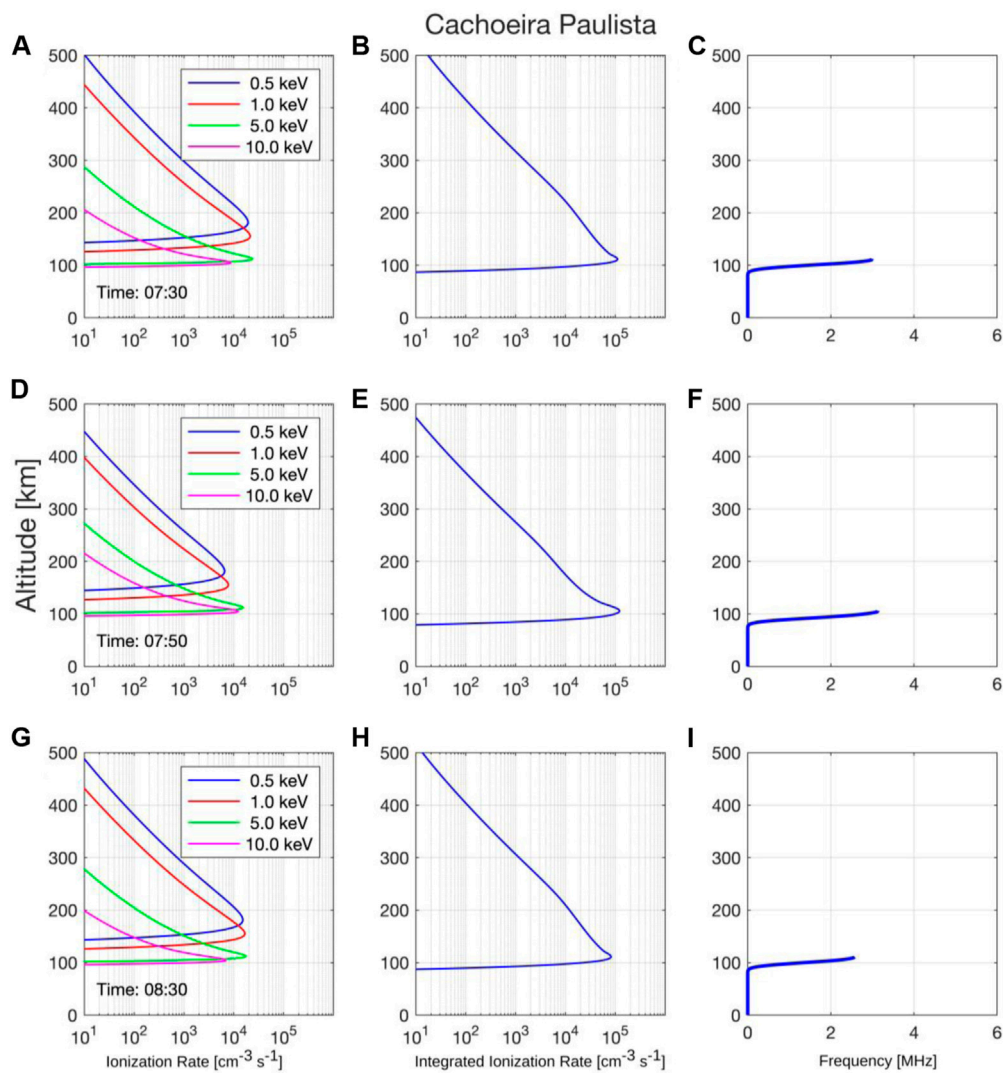


FIGURE 12

Ionization rate altitude profiles panels (A,D,G), ionization rate altitude integrated panels (B,E,H) and frequency range altitude panels (C,F,I) considering the second conjunction for Cachoeira Paulista station. The total incident energy of electrons is presented in Figure 10 (bottom panel). The ionization rate is obtained from empirical model (Fang et al., 2010) considering the total incident energy of electrons presented in Figure 10 (bottom panel) and the height scale presented in Figure 15 (bottom panel).

third (bottom panels) conjunctions. The Figure 7 (top panels) shows the ionograms considering the first conjunction period (01:36 UT and 01:44 UT), which occurs during the M-P. A flat trace is observed in the ionogram at 01:30 UT (short period) at around 120 km. This Es layer's type is classified as Es_f (Haldoupis, 2012). The ionograms show the absence of the Es_a layers in all the analyzed time, which means the absence of the low-energy EP effect over Cachoeira Paulista during the M-P. Supplementary Figure S2 (top panels) presents the absence of the Es layers in Santa Maria during the analyzed time. It is important to highlight that only the magnetosonic wave activities are detected during this conjunction within the inner radiation belt (Figure 5 - left panels).

The middle panels of Figure 7 show the ionograms considering the second conjunction period (07:40 UT and 07:42 UT), which occurs during the R-P (night time). A spread and diffuse trace is observed in the ionograms that performed a downward movement reaching 100–150 km. This Es layer's characteristic type is classified as Es_a layer (Moro et al., 2022; Resende et al., 2013; Kirkwood and Nilsson, 2000) and could be associated with the low-energy EP from the inner radiation belt (Batista and Abdu, 1977). Supplementary Figure S2 (middle panels) presents similar signatures in the ionograms registered in Santa Maria, which exhibit the Es_a layers characteristics during the analyzed time. The hiss and MS wave activities were

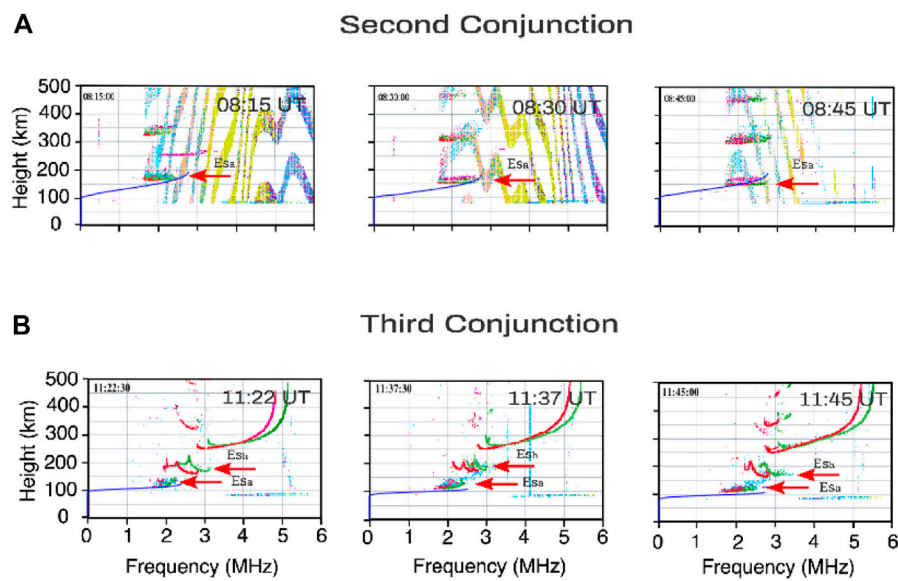


FIGURE 13

Ionograms from Digisonde located at Santa Maria during the second (A), and third (B) conjunctions. The red arrows show the E_{s_a} layer presence and the blue line is referent the plasma modeled frequency (MHz) altitude. Unfortunately, the Santa Maria ionograms present high 60 Hz interferences from the street lights used nearby the Digisonde site.

detected in the inner radiation belt (Figure 5 - right panels) during this second conjunction. The hiss waves are considered in the literature as important to cause the low-energy EP over the SAMA region during the R-P (Gonzalez et al., 1987). Thereby, it is crucial to investigate the dynamic mechanisms responsible for the low-energy EP driven by these waves, as described in.

Finally, Figure 7 (bottom panels) shows the ionograms from the Cachoeira Paulista station considering the third conjunction period (11:21 UT and 11:24 UT), which also occurs during the R-P (daytime). A trace discontinued in height with the E-region trace is observed in the ionograms, which descends with time, becoming a trace with a relatively symmetrical cusp at the peak of the E-region electron density (above 150 km). This signature in the ionograms is evidence of the E_{s_b} layer over SAMA during the R-P that could be associated with the strong wind shear. On the other hand, the weak spread and diffuse trace observed between 100 and 150 km exhibit very clear E_{s_a} layers characteristics. Furthermore, the E region appears strong, suggesting that the E region conductivity increased due to the particle precipitation (Santos et al., 2016). Supplementary Figure S2 (bottom panels) presents similar signatures in the ionograms registered in Santa Maria station, which shows the presence of the E_{s_b} layer and a weak spread and diffuse traces during the entire analyzed time that can be classified as E_{s_a} layer. Although the E_{s_a} layer is usually observed during the night hours (Hunsucker and Owren, 1962), and this third conjunction occurs in the morning

(around 08:30 LT), the evidences shown in the ionograms of the two stations give us the confidence to classify the layers as E_{s_a} . Moreover, the plasma wave activities within the inner radiation belt during the third conjunction are very similar to the second conjunction. Considering all these points, it is crucial to investigate the dynamic mechanisms responsible for the low-energy EP driven by these waves which will be done in the next sections.

Dynamic mechanisms responsible for the low-energy EP over SAMA during the second conjunction

According to the conjunctions observed during the M-P and R-P (Table 1) and the E_{s_a} layer detected in the ionosonde stations over the SAMA region (Figure 7), the coincidences between the E_{s_a} layer's signature and the conjunctions were observed during R-P, in the second and third conjunctions. Figure 8 highlights the second conjunction with the VAP-B orbit (white dotted line) and the Southern Hemisphere footprint (white dashed line) of May 28, and the ionosonde stations (red stars). The VAP-B orbit and their footprint are obtained at <https://sscweb.gsfc.nasa.gov/cgi-bin/Locator.cgi>. The magnetic equator (red line) and the global magnetic field (color's scale) obtained with International Geomagnetic Reference Field (IGRF-13th generation) (Alken et al., 2021) are also presented in Figure 8, in which the ionosonde stations are localized in the center of the SAMA

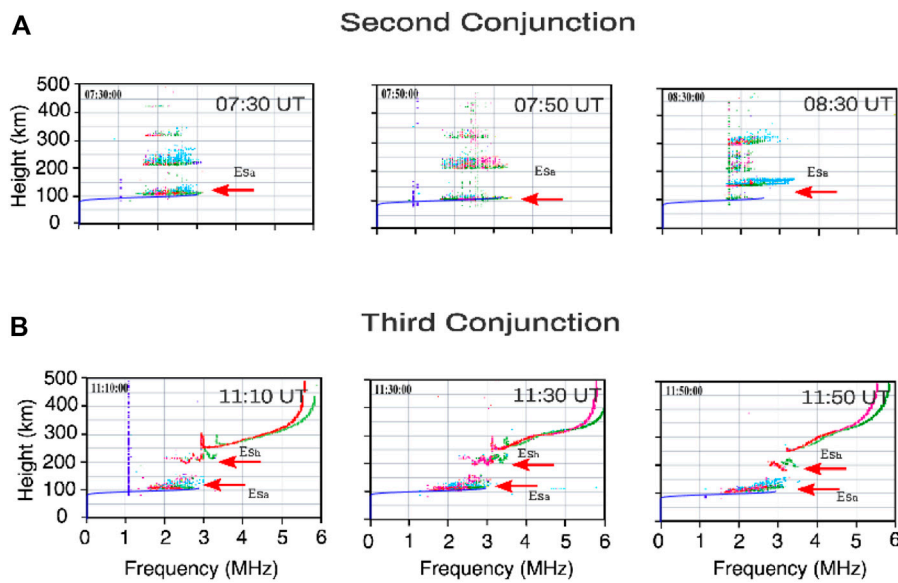


FIGURE 14 Ionograms from Digisonde located at Cachoeira Paulista during the second (A) and third (B) conjunctions. The red arrows show the Es_s layer presence and the blue line is referent the plasma modeled frequency (MHz) altitude.

region (22,000 nT isoline). The third conjunction with the VAP-A orbit and the Southern Hemisphere footprint of May 28, and the ionosonde stations are presented in [Supplementary Figure S3](#).

The plasma waves, such as hiss and MS waves are detected during this second conjunctions ([Figure 5](#) - right panels), and the Wave Normal Angle (WNA) is calculated through the singular value decomposition method ([Santolík et al., 2003](#)) to discuss the dynamic mechanisms responsible for the low-energy electron precipitation over the SAMA region. Hiss waves are widely distributed in the radial distance and magnetic local time (MLT) and can cause precipitation of electrons from tens of keV to a few MeV to the atmosphere through pitch angle scattering mechanism ([Meredith et al., 2006, 2007](#)). Pitch angle scattering is a resonant mechanism between the electrons and magnetospheric waves, in which the first adiabatic invariant (μ), that depends on the particle's pitch angle and its energy, is violated (e.g., [Baumjohann and Treumann, 2012; Hartley and Denton, 2014](#)). Conversely, the MS wave activities are mainly confined to the geomagnetic equator and propagate perpendicular to the background magnetic field. The MS waves can scatter the electrons from high pitch angles (close to 90°) to intermediate pitch angles ([Xiao et al., 2015](#)) due to the resonance conditions. [Shklyar and Matsumoto \(2009\)](#) showed two resonance conditions for electrons, named cyclotron resonance and Landau resonance, respectively:

$$v_{\parallel} = \frac{\omega - f_{ce}}{k_{\parallel}}, \tag{1}$$

$$v_{\parallel} = \frac{\omega}{k_{\parallel}}, \tag{2}$$

where k_{\parallel} and v_{\parallel} are parallel components of the wave normal vector and charged particle velocity, respectively. ω is wave frequency, and f_{ce} is the magnitude of the electron cyclotron frequency in the relations which are specific for electrons. These conditions require large parallel velocity once the k_{\parallel} is very small, and thus, a small pitch angle.

[Figure 9](#) presents the frequency-time spectrogram of magnetic field (panel a), WNA (panel b), frequency ratio f_{pe}/f_{ce} (panel c - blue line), and total electron density inferred from the upper hybrid resonance line (panel c - black line). The $fLHR$ (yellow line) are presented in panel a. During the plasmaspheric hiss wave activities (from 08:08 UT) is observed $WNA \leq 40^\circ$, as also observed by [Li et al. \(2015\)](#). Unlike hiss waves, the propagation of MS waves is highly oblique related to ambient magnetic field direction and linearly polarized ([Horne et al., 2007; Ma et al., 2016](#)), i.e., $WNA \geq 70^\circ$ from 07:56 UT.

The frequency ratio f_{pe}/f_{ce} (panel c—blue line) presents low values $\sim 2 - 3$ from $\sim 08:08$ UT, as expected when the plasmopause is located at $L \sim 1.8$ (see [Albert et al., 2016; Watt et al., 2019](#)). The resonant energy for whistler mode waves propagating parallel to the ambient magnetic field interacting with keV electrons is a function of the electron gyrofrequency (f_{ce}) and the plasma frequency (f_{pe}), besides the wave frequency (f), the speed of light (c) and the electron rest mass (m_e) (e.g., [Helliwell, 1965; Malykhin et al., 2021](#)).

$$Wr = \frac{m_e c^2}{f} \frac{(f_{ce} - f)^3}{f_{pe}^2}, \tag{3}$$

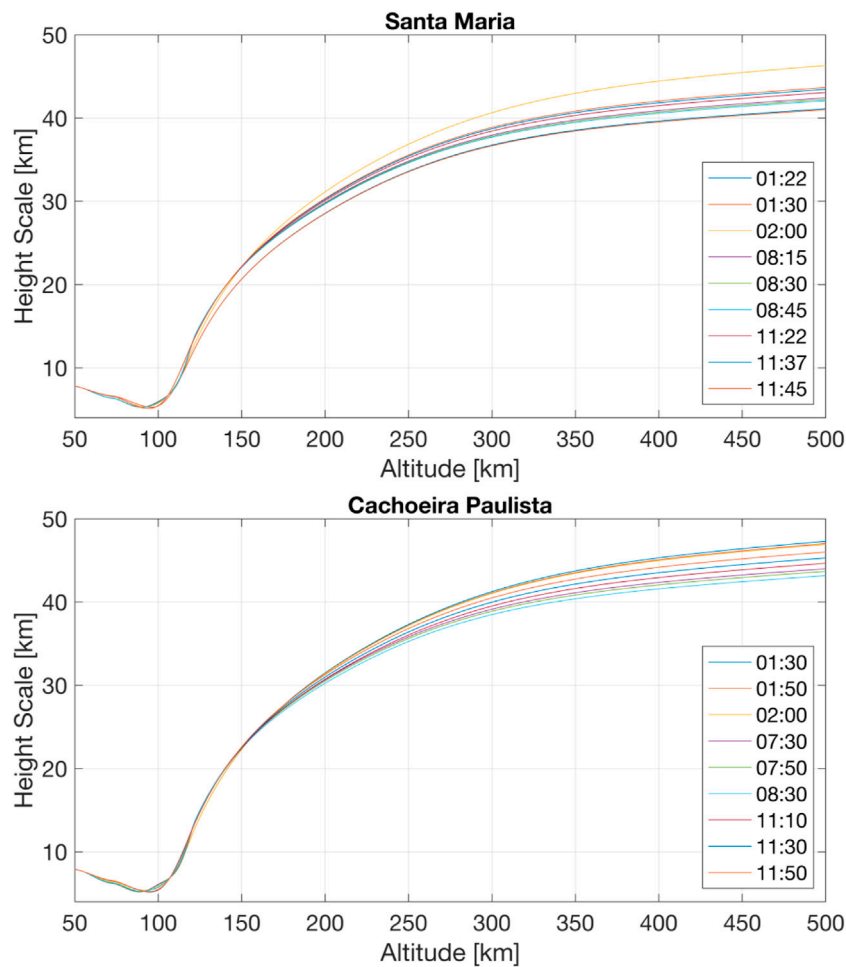


FIGURE 15
Height scale (km) for Santa Maria (top) and Cachoeira Paulista (bottom) stations, considering the three conjunctions.

Accordingly, the resonant energy is a function of the ambient plasma density and magnetic field strength, and by further calculation it can be shown that it increases following the decrease of f_{pe}/f_{ce} ratio. Thus, the low values of the frequency ratio (f_{pe}/f_{ce}) can be efficient for scattering loss of electrons (hundreds of keV) driven by MS waves (see [Lei et al., 2017](#)). However, we are interested in low-energy EP (tens of keV) because this energy range can generate the E_s layers over SAMA ([Batista and Abdu, 1977](#)). Thereby, the results presented here suggest that the hiss waves may cause the scattering loss of electrons (tens of keV) over this region. Additionally, it is essential to highlight the results observed in [Figure 4](#) (panel d), especially during the second conjunction, in which the quasi-linear scattering time scale $1/D_{aa}$ (10 keV) is below 1 h, presumably causing intensive precipitations of 10 keV electrons to the ionosphere over the SAMA region.

Atmospheric ionization over SAMA (100–150 km) induced by low-energy EP

An empirical model with a new parameterization of ionization in the atmosphere by the isotropically precipitating electrons (100 eV–1 MeV) ([Fang et al., 2010](#)) is used here to estimate the atmospheric ionization over SAMA during the second and third conjunctions induced by low-energy EP. To compute the atmospheric ionization, we assume that the incident particles (differential number flux, $\text{cm}^{-2} \text{s}^{-1} \text{keV}^{-1}$) have a Maxwellian distribution defined by the function:

$$\Phi_M(E) = \frac{Q_0}{2E_0^3} E \exp\left(-\frac{E}{E_0}\right), \quad (4)$$

where the free parameters are total energy flux (Q_0 , $\text{keV cm}^{-2} \text{s}^{-1}$) and the characteristic energy (E_0 , keV). The differential number flux

(Φ_M) is given in $\text{cm}^{-2} \text{s}^{-1} \text{keV}^{-1}$. Figure 10 shows the total incident energy of electrons (100 eV—hundreds of keV) for Santa Maria (top) and Cachoeira Paulista (bottom) stations, considering the second and third conjunctions. The orders of magnitude of the total incident energy of electrons in Santa Maria are tens of keV and hundreds of keV during the second and third conjunctions, respectively. Otherside, the orders of magnitude of the total incident energy of electrons in Cachoeira Paulista are hundreds of keV during the second and third conjunctions.

$$H(z) = \frac{kT(z)}{m(z)g(z)}, \quad (5)$$

where k is the Boltzmann constant, T is the atmospheric temperature, m is the average molecular weight, g is the acceleration due to the gravity and z is vertical location.

The ionization model data (Fang et al., 2010) also estimates the plasma frequency (MHz) altitude profile. First, it is considered that the time variation of electronic density ($\frac{\partial N_e}{\partial t}$) is equal to the difference between the ionization rate (Φ_M) and the loss terms. After that, the electron density is obtained assuming that the loss terms are proportional to the population ($\frac{N_e}{\tau}$) and assuming a short-time scale for the recombination (τ), which the transport mechanisms can be neglected. Here, we assume a recombination time (τ) of 1 s (Batista and Abdu, 1977), and then the plasma frequency (MHz) altitude profile is obtained. This plasma frequency is the highest cutoff frequency at which the ionosphere layers reflect electromagnetic waves (Kumluca et al., 1999), which in turn, is associated with the peak electron concentration of the Es layer, N_e (electrons/ m^3) by the simple relation $F_c = c\sqrt{N_e}$, where $c = 8.98$ (e.g., Yu et al., 2020; Nikolaeva et al., 2021).

Figures 11, 12 present the ionization rate altitude profiles (panels a, d, g), ionization rate altitude integrated between 100 eV and 100 keV (panels b, e, h), and the plasma modeled frequency (MHz) altitude profile (panels c, f, i) during the second conjunction. Figures 11, 12 are referring to Santa Maria and Cachoeira Paulista stations, respectively. Profiles of the ionization rate for four different energy levels of the electrons (0.5 keV (blue line), 1.0 keV (red line), 5.0 keV (green line), and 10 keV (magenta line)) are given in Figures 11, 12, panels a,d,g. At both ionosonde stations, the ionization rate peaks between 100–200 km altitude for all different energy levels, while the maximum of the low-energy electrons between 0.5–1.0 keV is generally located at higher altitudes compared to the low-energy electrons between 5.0–10.0 keV. The altitude integrated ionization rate (panels b, e, h) provides the energy amount deposited in the $100 \text{ km} \leq \text{altitude} \leq 200 \text{ km}$. The Es_a layer density due the electron precipitation can be identified in panels (c), (f), and (i), which were estimated through the calculation of the modeled plasma frequency in (MHz). The ionization rate observed in Figures 11, 12 suggests the occurrences of the low-energy EP (0.5–10 keV) over the SAMA region during the Es_a layer generation, as expected the low-energy EP ($\geq 10 \text{ keV}$) occurred due to pitch angle scattering driven by plasmaspheric hiss waves discussed in previous sections. Although the previous studies of hiss waves have

been focused on the scattering of electrons of 10 keV - 1 MeV energies, the recent studies (Li J. et al., 2019; Khazanov and Ma 2021) have shown that the hiss waves also can scatter electrons of energies below several keV down to the energies of tens of eV. The Es_a layer which occurs in Santa Maria is considerably higher than the Es_a layer in Cachoeira Paulista. This behavior can be attributed to the low ionization rate due to the low-energy EP = 5 and 10 keV in Santa Maria. Therefore, we suggest that the low-energy EP $\leq 1 \text{ keV}$ is the main ingredient to generate Es_a layer detected close to 150 km altitude in Santa Maria, while the low-energy EP $\leq 10 \text{ keV}$ is the main ingredient to generate Es_a layer detected close to 100–120 km altitude in Cachoeira Paulista.

The ionization rate altitude profiles, ionization rate altitude integrated, and the plasma modeled frequency altitude during the third conjunction are presented in the support information, Supplementary Figure S4 (Santa Maria station) and Supplementary Figure S5 (Cachoeira Paulista station). The ionization rate observed in Supplementary Figure S4, S5 suggests the occurrences of the low-energy electron precipitation over the SAMA region during the third conjunction due to pitch angle scattering driven by plasmaspheric hiss waves.

We can estimate the free parameters (Q_0 , E_0) by comparing these plasma frequencies (MHz) altitude profile modeled with the Es_a layers presented in the ionograms, as shown in Figures 13, 14.

Finally, although the downward movement to be typical in low/mid-latitudes due to the wind shear mechanism (Resende et al., 2017), the inner radiation belt dynamic and the atmospheric ionization over SAMA are highly favorable to the occurrences of the low-energy EP during the second (Figures 13, 14 - middle panels) and third (Figures 13, 14 - bottom panels) conjunctions. It means that this atmospheric ionization over SAMA, especially in 100–150 km altitude, is very similar to the ionized atmosphere in the auroral region during the generation of the Es_a layers (Whalen et al., 1971; Buchau et al., 1972; Blagoveshchensky and Borisova, 2000). Therefore, we can suggest that the low-energy EP ($\leq 10 \text{ keV}$) from the inner radiation belt is the main ingredient responsible for generating the Es_a layers over Cachoeira Paulista during the R-P at nighttime Figure 15. Conversely, the low-energy EP ($\leq 1 \text{ keV}$) is the main ingredient responsible for generating the Es_a layers over Santa Maria during the R-P at night.

Concluding remarks

The hiss wave's power spectral density and the ambient plasma conditions as given by the low values of the frequency ratio f_{pe}/f_{ce} suggests the occurrences of the low-energy EP ($\geq 10 \text{ keV}$) to the atmosphere during the recovery phase of a geomagnetic storm. Additionally, the modeling results

(Figure 4D) show that the quasi-linear scattering time scale $1/D_{aa}$ (10 keV) is below 1 h, especially during the second conjunction. It suggests that the quasi-linear scattering driven by hiss waves is one of the causes of the intensive precipitations of 10 keV electrons to the ionosphere over the SAMA region.

The estimation of the atmospheric ionization induced by low-energy EP over SAMA suggests the deposition of the electrons (≤ 10 keV) at altitudes 100–120 km. Therefore, we can suggest that the pitch angle scattering driven by hiss waves triggers the dynamic mechanism responsible for the low-energy electron precipitation over the SAMA region that generates and maintains the E_s layer in this low latitude during the recovery phase geomagnetic storm. Otherwise, atmospheric ionization induced by the low-energy EP over SAMA also suggests the deposition of the electrons (≤ 1 keV) in altitudes from 150 km, which was decisive to the E_s layer occurrence at 150 km in Santa Maria.

The techniques used here, such as the observational and modeled data analyses, contribute to explaining the coupling between the inner radiation belt and the ionized atmosphere over the SAMA region, which was not well understood before. Additionally, the signature of this atypical E_s layer in the Brazilian sites could be used as an indicator of the occurrences of the low-energy electron precipitation over SAMA once the electron detectors onboard of the low orbit satellites are contaminated with the proton flux trapped in the inner belt (e.g., Rodger et al., 2013; Andersson et al., 2014).

Data availability statement

The raw data supporting the conclusions of this article will be made available by the authors, without undue reservation.

Author contributions

LD, LR, OA, CA, and LV contributed to conception and design of the study. VD and JM organized the database. LD, VD, JM, OA, LA, FC, PJ, CM, MA and WG analyzed the Interplanetary medium conditions and magnetospheric conditions. JS, LR, IB, CA, CW, JM, SC, ZL and CD interpreted the ionospheric data. LV modeled the Atmospheric ionization over SAMA. LD wrote the first draft of the manuscript. All authors contributed to manuscript revision, read, and approved the submitted version.

Funding

This research was also supported by the National Natural Science Foundation of China (42074201 and 41674145), by the International Partnership Program of Chinese Academy of Sciences

(grants 183311KYSB20200003 and 183311KYSB20200017). MA thanks CNPq/MCTIC (310900/2016-6). LV thanks CNPq/MCTIC (Grants 307404/2016-1), TED-004/2020-AEB and PO-20VB.0009. LA thanks to CNPq/MCTIC (301476/2018-7). IB thanks CNPq/MCTI, grants 405555/2018-0 and 306844/2019-2. JM would like to thank the CNPq/MCTIC (grant 429517/2018-01). SC thanks CAPES/MEC (grant 88887.362982/2019-00). CD thanks CNPq/MCTI by grants 303643/2017-0. OA was supported by NASA grants 80NNSC19K0264, 80NNSC19K0848, 80NNSC20K0218, 80NNSC22K0522, and NSF grant 1914670. Christina Arras acknowledges the support through Deutsche Forschungsgemeinschaft (DFG) within the DFG Priority Program DynamicEarth, SPP 1788.

Acknowledgments

We acknowledge the NASA Van Allen Probes, Harlan E. Spence [PI ECT; University of New Hampshire], Craig Kletzing [PI EMFISIS; University of Iowa] and John R. Wygant [PI EFW; University Minnesota] for use of data. We acknowledge the NASA ACE satellite, Edward Stone [PI ACE; Caltech]. LD, LR, JM, PJ, JM, and WG are grateful for financial support from China-Brazil Joint Laboratory for Space Weather. LD is grateful to Aaron Hendry and Rodger Craig (University of Otago) for the discussions regarding particle precipitation over SAMA using the POES satellite data. LD also thanks Graziela Belmiro (INPE) for the discussions about the outer radiation belt.

Conflict of interest

The authors declare that the research was conducted in the absence of any commercial or financial relationships that could be construed as a potential conflict of interest.

Publisher's note

All claims expressed in this article are solely those of the authors and do not necessarily represent those of their affiliated organizations, or those of the publisher, the editors and the reviewers. Any product that may be evaluated in this article, or claim that may be made by its manufacturer, is not guaranteed or endorsed by the publisher.

Supplementary material

The Supplementary Material for this article can be found online at: <https://www.frontiersin.org/articles/10.3389/fspas.2022.970308/full#supplementary-material>

References

- Abel, B., and Thorne, R. M. (1998). Electron scattering loss in Earth's inner magnetosphere: 1. Dominant physical processes. *J. Geophys. Res.* 103 (A2), 2385–2396. doi:10.1029/97JA02919
- Agapitov, O., Artemyev, A. V., Mourenas, D., Mozer, F. S., and Krasnoselskikh, V. (2015). Empirical model of lower band chorus wave distribution in the outer radiation belt. *JGR. Space Phys.* 120, 10425–10442. doi:10.1002/2015JA021829
- Agapitov, O., Mourenas, D., Artemyev, A., Claudepierre, S. G., Hospodarsky, G., and Bonnell, J. W. (2020). Lifetimes of relativistic electrons as determined from plasmaspheric hiss scattering rates statistics: Effects of ω_p/ω_{ce} and wave frequency dependence on geomagnetic activity. *Geophys. Res. Lett.* 47. doi:10.1029/2020gl088052
- Agapitov, O., Mourenas, D., Artemyev, A., Hospodarsky, G., and Bonnell, J. W. (2019). Time scales for electron quasi-linear diffusion by lower-band chorus waves: The effects of ω_p/ω_{ce} dependence on geomagnetic activity. *Geophys. Res. Lett.* 0 (0), 6178–6187. doi:10.1029/2019GL083446
- Agapitov, O. V., Mourenas, D., Artemyev, A. V., Mozer, F. S., Hospodarsky, G., Bonnell, J., et al. (2018). Synthetic empirical chorus wave model from combined van allen probes and cluster statistics. *JGR. Space Phys.* 123 (1), 297–314. doi:10.1002/2017JA024843
- Albert, J. M., Starks, M. J., Horne, R. B., Meredith, N. P., and Glauert, S. A. (2016). Quasi-linear simulations of inner radiation belt electron pitch angle and energy distributions. *Geophys. Res. Lett.* 43, 2381–2388. doi:10.1002/2016GL067938
- Alken, P., Thébault, E., Beggan, C. D., Amit, H., Aubert, J., Baerenzung, J., et al. (2021). International geomagnetic reference field: The thirteenth generation. *Earth Planets Space* 73 (1), 49. doi:10.1186/s40623-020-01288-x
- Andersson, M. E., Verronen, P. T., Rodger, C. J., Clilverd, M. A., and Wang, S. (2014). Longitudinal hotspots in the mesospheric OH variations due to energetic electron precipitation. *Atmos. Chem. Phys.* 14 (2), 1095–1105. doi:10.5194/acp-14-1095-2014
- Batista, I. S., and Abdu, M. A. (1977). Magnetic storm associated delayed sporadic E enhancements in the Brazilian Geomagnetic Anomaly. *J. Geophys. Res.* 82 (29), 4777–4783. doi:10.1029/JA082i029p04777
- Baumjohann, W., and Treumann, R. A. (2012). *Basic space plasma physics: Revised edition. Basic space plasma Physics*. Revised Edition. World Scientific. doi:10.1142/P850
- Blagoveshchensky, D. V., and Borisova, T. D. (2000). Substorm effects of ionosphere and HF propagation. *Radio Sci.* 35 (5), 1165–1171. doi:10.1029/1998RS001776
- Blake, J. B., Carranza, P. A., Claudepierre, S. G., Clemmons, J. H., Crain, W. R., Jr, Dotan, Y., et al. (2013). The magnetic electron ion spectrometer (MagEIS) instruments aboard the radiation belt storm probes (RBSP) spacecraft. *Space Sci. Rev.* 179, 383–421. doi:10.1007/s11214-013-9991-8
- Blum, L. W., Schiller, Q., Li, X., Millan, R., Halford, A., and Woodger, L. (2013). New conjunctive CubeSat and balloon measurements to quantify rapid energetic electron precipitation. *Geophys. Res. Lett.* 40, 5833–5837. doi:10.1002/2013GL058546
- Boardsen, S. A., Hospodarsky, G. B., Kletzing, C. A., Engebretson, M. J., Pfaff, R. F., Wygant, J. R., et al. (2016). Survey of the frequency dependent latitudinal distribution of the fast magnetosonic wave mode from Van Allen Probes Electric and Magnetic Field Instrument and Integrated Science waveform plasma wave analysis. *J. Geophys. Res. Space Phys.* 121 (4), 2902–2921. doi:10.1002/2015JA021844
- Bortnik, J., Thorne, R. M., Ni, B., and Li, J. (2015). Analytical approximation of transit time scattering due to magnetosonic waves. *Geophys. Res. Lett.* 42, 1318–1325. doi:10.1002/2014GL062710
- Bortnik, J., and Thorne, R. M. (2010). Transit time scattering of energetic electrons due to equatorially confined magnetosonic waves. *J. Geophys. Res.* 115, A07213. doi:10.1029/2010JA015283
- Buchau, J., Gasman, G. J., Pike, C. P., Wagner, R. A., and Whalen, J. A. (1972). Precipitation patterns in the Arctic ionosphere determined from inner radiation belt observations. *Ann. Geophys.* 28, 443–453.
- Cai, H.-T., and Ma, S.-Y. (2007). Initial study of inversion method for estimating energy spectra of auroral precipitating particles from ground-based is radar observations. *Chin. J. Geophys.* 50 (1), 12–21. doi:10.1002/cjg2.1005
- Cane, H. V., and Richardson, I. G. (2003). Interplanetary coronal mass ejections in the near-Earth solar wind during 1996–2002. *J. Geophys. Res.* 108 (A4), 1156. doi:10.1029/2002JA009817
- Cao, J. B., Liu, Z. X., Yang, J. Y., Yian, C. X., Wang, Z. G., Zhang, X. H., et al. (2005). First results of low frequency electromagnetic wave detector of TC-2/ Double Star program. *Ann. Geophys.* 23 (8), 2803–2811. doi:10.5194/angeo-23-2803-2005
- Chappell, C., Harris, K., and Sharp, G. (1970). A study of the influence of magnetic activity on the location of the plasmopause as measured byOGO 5. *J. Geophys. Res.* 75 (1), 50–56. doi:10.1029/JA075i001p00050
- Chen, L., Maldonado, A., Bortnik, J., Thorne, R. M., Li, J., Dai, L., et al. (2015). Nonlinear bounce resonances between magnetosonic waves and equatorially mirroring electrons. *JGR. Space Phys.* 120 (8), 6514–6527. doi:10.1002/2015JA021174
- Claudepierre, S. G., O'Brien, T. P., Blake, J. B., Fennell, J. F., Roeder, J. L., Clemmons, J. H., et al. (2015). A background correction algorithm for Van Allen Probes MagEIS electron flux measurements. *JGR. Space Phys.* 120, 5703–5727. doi:10.1002/2015JA021171
- Da Silva, L. A., Shi, J., Alves, L. R., Sibeck, D., Souza, V. M., Marchezi, J. P., et al. (2021). Dynamic mechanisms associated with high-energy electron flux dropout in the Earth's outer radiation belt under the influence of a coronal mass ejection sheath region. *JGR. Space Phys.* 126 (1), 2020JA028492. doi:10.1029/2020JA028492
- Denardini, C. M., Dasso, S., and Gonzalez-Esparza, J. A. (2016). Review on space weather in Latin America. 2. The research networks ready for space weather. *Adv. Space Res.* 58 (10), 1940–1959. doi:10.1016/j.asr.2016.03.013
- Echer, E., Gonzalez, W. D., Tsurutani, B. T., and Gonzalez, A. L. C. (2008). Interplanetary conditions causing intense geomagnetic storms ($Dst \leq -100$ nT) during solar cycle 23 (1996–2006). *J. Geophys. Res.* 113, A05221. doi:10.1029/2007JA012744
- Fang, X., Randall, C. E., Lummerzheim, D., Wang, W., Lu, G., Solomon, S. C., et al. (2010). Parameterization of monoenergetic electron impact ionization. *Geophys. Res. Lett.* 37, L22106. doi:10.1029/2010GL045406
- Goldstein, J. (2006). "Plasmasphere response: Tutorial and review of recent imaging results," in *Solar dynamics and its effects on the heliosphere and Earth* (Springer), 203–216. doi:10.1007/978-0-387-69532-7_14
- Gonzalez, W. D., Dutra, S. L. G., and Pinto, O. (1987). Middle atmospheric electrodynamic modification by particle precipitation at the South Atlantic Magnetic Anomaly. *J. Atmos. Terr. Phys.* 49 (4), 377–383. doi:10.1016/0021-9169(87)90032-8
- Gonzalez, W. D., Joselyn, J. A., Kamide, Y., Kroehl, H. W., Rostoker, G., Tsurutani, B. T., et al. (1994). What is a geomagnetic storm? *J. Geophys. Res.* 99, 5771. doi:10.1029/93JA02867
- Gonzalez, W. D., Tsurutani, B. T., and Clúa De Gonzalez, A. L. (1999). Interplanetary origin of geomagnetic storms. *Space Sci. Rev.* 88 (3–4), 529–562. doi:10.1023/a:1005160129098
- Green, A., Li, W., Ma, Q., Shen, X.-C., Bortnik, J., and Hospodarsky, G. B. (2020). Properties of lightning generated whistlers based on Van Allen Probes observations and their global effects on radiation belt electron loss. *Geophys. Res. Lett.* 47, e2020GL089584. doi:10.1029/2020GL089584
- Green, J. L., Boardsen, S., Garcia, L., Taylor, W. W., Fung, S. F., and Reinisch, B. W. (2005). On the origin of whistler mode radiation in the plasmasphere. *J. Geophys. Res.* 110, A03201. doi:10.1029/2004JA010495
- Guo, D., Fu, S., Xiang, Z., Ni, B., Guo, Y., Feng, M., et al. (2021). Prediction of dynamic plasmopause location using a neural network. *Space weather.* 19. doi:10.1029/2020SW002622
- Haldoupis, C. (2012). Midlatitude sporadic E. A typical paradigm of atmosphere-ionosphere coupling. *Space Sci. Rev.* 168, 441–461. doi:10.1007/s11214-011-9786-8
- Hartley, D. P., and Denton, M. H. (2014). Solving the radiation belt riddle. *Astronomy Geophys.* 55 (6), 6.17–6.20. doi:10.1093/astrogeof/atu247
- Hartley, D. P., Kletzing, C. A., Santolik, O., Chen, L., and Horne, R. B. (2018). Statistical properties of plasmaspheric hiss from Van Allen Probes observations. *JGR. Space Phys.* 123, 2605–2619. doi:10.1002/2017JA024593
- Helliwell, R. A. (1965). *Whistlers and related ionospheric phenomena*. Stanford University Press.
- Horne, R. B., Thorne, R. M., Glauert, S. A., Meredith, N. P., Pokhotelov, D., and Santolik, O. (2007). Electron acceleration in the Van Allen radiation belts by fast magnetosonic waves. *Geophys. Res. Lett.* 34, L17107. doi:10.1029/2007GL030267
- Hunsucker, R. D., and Owren, L. (1962). Auroral sporadic-E ionization. *J. Res. Natl. Bureau Standards-D. Radio Propag.* 66D (5), 581. doi:10.6028/jres.066d.057
- Inan, U. S., Walt, M., Voss, H. D., and Imhof, W. L. (1989). Energy spectra and pitch angle distributions of lightning-induced electron precipitation: Analysis of an event observed on the S81-1 (SEEP) satellite. *J. Geophys. Res.* 94, 1379–1401. doi:10.1029/ja094ia02p01379

- Khazanov, G. V., and Ma, Q. (2021). Dayside low energy electron precipitation driven by hiss waves in the presence of ionospheric photoelectrons. *JGR. Space Phys.* 126, e2021JA030048. doi:10.1029/2021JA030048
- Kirkwood, S., and Nilsson, H. (2000). High-latitude sporadic-E and other thin layers – the role of magnetospheric electric fields. *Space Sci. Rev.* 91, 579–613. doi:10.1023/A:1005241931650
- Kletzing, C. A., Kurth, W. S., Acuna, M., MacDowall, R. J., Torbert, R. B., Averkamp, T., et al. (2013). The electric and magnetic field instrument suite and integrated science (EMFISIS) on RBSP. *Space Sci. Rev.* 179 (1–4), 127–181. doi:10.1007/s11214-013-9993-6
- Kumluca, A., Tulunay, E., Topalil, I., and Tulunay, Y. (1999). Temporal and spatial forecasting of ionospheric critical frequency using neural networks. *Radio Sci.* 34 (6), 1497–1506. doi:10.1029/1999rs900070
- Kurth, W. S., De Pascuale, S., Faden, J. B., Kletzing, C. A., Hospodarsky, G. B., Thaller, S., et al. (2015). Electron densities inferred from plasma wave spectra obtained by the Waves instrument on Van Allen Probes. *JGR. Space Phys.* 120, 904–914. doi:10.1002/2014JA020857
- Kuznetsov, V. D. (2007). From the geophysical to heliophysical year: The results of the coronas-F project. *Russ. J. Earth Sci.* 9, 1–14. doi:10.2205/2007ES000276
- Laakso, H., Junginger, H., Roux, A., Schmidt, R., and de Villedary, C. (1990). Magnetosonic waves above $f_c(H^+)$ at geostationary orbit: GEOS 2 results. *J. Geophys. Res.* 95, 10609. doi:10.1029/ja095ia07p10609
- Lei, M., Xie, L., Li, J., Pu, Z., Fu, S., Ni, B., et al. (2017). The radiation belt electron scattering by magnetosonic wave: Dependence on Key parameters. *J. Geophys. Res. Space Phys.* 122 (12), 12338–12352. doi:10.1002/2016JA023801
- Lemaire, J. F., Gringauz, K. I., Carpenter, D. L., and Bassolo, V. (1988). *The Earth's Plasmasphere*. New York: Cambridge Univ. Press
- Li, J., Ma, Q., Bortnik, J., Li, W., An, X., Reeves, G. D., et al. (2019a). Parallel acceleration of suprathermal electrons caused by whistler-mode hiss waves. *Geophys. Res. Lett.* 46, 12675. doi:10.1029/2019GL085562
- Li, J., Ni, B., Xie, L., Pu, Z., Bortnik, J., Thorne, R. M., et al. (2014). Interactions between magnetosonic waves and radiation belt electrons: Comparisons of quasi-linear calculations with test particle simulations. *Geophys. Res. Lett.* 41, 4828–4834. doi:10.1002/2014GL060461
- Li, W., Ma, Q., Thorne, R. M., Bortnik, J., Kletzing, C. A., Kurth, W. S., et al. (2015). Statistical properties of plasmaspheric hiss derived from Van Allen Probes data and their effects on radiation belt electron dynamics. *JGR. Space Phys.* 120 (5), 3393–3405. doi:10.1002/2015JA021048
- Li, W., Shen, X. C., Ma, Q., Capannolo, L., Shi, R., Redmon, R. J., et al. (2019b). Quantification of energetic electron precipitation driven by plume whistler mode waves, plasmaspheric hiss, and exohiss. *Geophys. Res. Lett.* 46 (7), 3615–3624. doi:10.1029/2019GL082095
- Liu, X., Liu, W., Cao, J. B., Fu, H. S., Yu, J., and Li, X. (2015). Dynamic plasmopause model based on THEMIS measurements. *J. Geophys. Res. Space Phys.* 120, 10543–10556. doi:10.1002/2015JA021801
- Lyons, L. R., Thorne, R. M., and Kennel, C. F. (1972). Pitch-angle diffusion of radiation belt electrons within the plasmasphere. *J. Geophys. Res.* 77 (19), 3455–3474. doi:10.1029/ja077i019p03455
- Ma, Q., Li, W., Thorne, R. M., and Angelopoulos, V. (2013). Global distribution of equatorial magnetosonic waves observed by THEMIS. *Geophys. Res. Lett.* 40 (10), 1895–1901. doi:10.1002/grl.50434
- Ma, Q., Li, W., Thorne, R. M., Bortnik, J., Kletzing, C. A., Kurth, W. S., et al. (2016). Electron scattering by magnetosonic waves in the inner magnetosphere. *JGR. Space Phys.* 121 (1), 274–285. doi:10.1002/2015JA021992
- Ma, Q., Li, W., Thorne, R. M., Bortnik, J., Reeves, G. D., Kletzing, C. A., et al. (2016b). Characteristic energy range of electron scattering due to plasmaspheric hiss. *JGR. Space Phys.* 121, 11,737–11,749. doi:10.1002/2016JA023311
- Maldonado, A. A., Chen, L., Claudepierre, S. G., Bortnik, J., Thorne, R. M., and Spence, H. (2016). Electron butterfly distribution modulation by magnetosonic waves. *Geophys. Res. Lett.* 43 (7), 3051–3059. doi:10.1002/2016GL068161
- Maldonado, A. A., and Chen, L. (2018). On the diffusion rates of electron bounce resonant scattering by magnetosonic waves. *Geophys. Res. Lett.* 45 (8), 3328–3337. doi:10.1002/2017GL076560
- Malykhin, A. Y., Grigorenko, E. E., Shklyar, D. R., Panov, E. V., Le Contel, O., Avakov, L., et al. (2021). Characteristics of resonant electrons interacting with whistler waves in the nearest dipolarizing magnetotail. *JGR. Space Phys.* 126, e2021JA029440. doi:10.1029/2021JA029440
- Mauk, B. H., Fox, N. J., Kanekal, S. G., Kessel, R. L., Sibeck, D. G., and Ukhorskiy, A. (2013). Science objectives and rationale for the radiation belt storm probes mission. *Space Sci. Rev.* 179 (1–4), 3–27. doi:10.1007/s11214-012-9908-y
- Meredith, N. P., Horne, R. B., Clilverd, M. A., Horsfall, D., Thorne, R. M., and Anderson, R. R. (2006). Origins of plasmaspheric hiss. *J. Geophys. Res.* 111 (9), A09217. doi:10.1029/2006JA011707
- Meredith, N. P., Horne, R. B., Glauert, S. A., and Anderson, R. R. (2007). Slot region electron loss timescales due to plasmaspheric hiss and lightning-generated whistlers. *J. Geophys. Res.* 112, A08214. doi:10.1029/2007JA012413
- Meredith, N. P., Horne, R. B., Thorne, R. M., Summers, D., and Anderson, R. R. (2004). Substorm dependence of plasmaspheric hiss. *J. Geophys. Res.* 109, A06209. doi:10.1029/2004JA010387
- Moro, J., Xu, J., Denardini, C. M., Resende, L. C. A., Silva, R. P., Liu, Z., et al. (2019). On the sources of the ionospheric variability in the South American magnetic anomaly during solar minimum. *J. Geophys. Res. Space Phys.* 124 (9), 7638–7653. doi:10.1029/2019JA026780
- Moro, J., Xu, J., Denardini, C. M., Resende, L. C. A., Da Silva, L. A., Chen, S. S., et al. (2022). Different Sporadic-E (Es) layer types development during the August 2018 geomagnetic storm: Evidence of Auroral Type (Esa) over the SAMA region. *J. Geophys. Res. Space Phys.* 127 (2). doi:10.1029/2021JA029701
- Nath, N., Steen Mikkelsen, I., and Stockflet Jørgensen, T. (1980). On the formation of high latitude Es-layers. *J. Atmos. Terr. Phys.* 42 (9–10), 841–852. doi:10.1016/0021-9169(80)90088-4
- Nikolaeva, V., Gordeev, E., Sergienko, T., Makarova, L., and Kotikov, A. (2021). AIM-E: E-Region auroral ionosphere model. *Atmosphere* 12, 748. doi:10.3390/atmos12060748
- Nishino, M., Makita, K., Yumoto, K., Miyoshi, Y., Schuch, N. J., and Abdu, M. A. (2006). Energetic particle precipitation in the Brazilian geomagnetic anomaly during the “Bastille day storm” of July 2000. *Earth Planets Space* 58 (5), 607–616. doi:10.1186/bf03351958
- Paulikas, G. A. (1975). Precipitation of particles at low and middle latitudes. *Rev. Geophys.* 13, 709–734. doi:10.1029/rg013i005p0709
- Pierrard, V., Khazanov, G., Cabrera, J., and Lemaire, J. (2008). Influence of the convection electric field models on predicted plasmopause positions during magnetic storms. *J. Geophys. Res.* 113 (A8). doi:10.1029/2007JA012612
- Piggott, W. R., and Rawer, K. (1978). *U.R.S.I. Handbook of ionogram interpretation and reduction*. Second edition. Boulder, Colorado: World Data Center A for Solar-Terrestrial Physics. Report UAG-23NOAA.
- Pinto, O., and Gonzalez, W. D. (1989). Energetic electron precipitation at the South Atlantic magnetic anomaly: a review. *J. Atmos. Terr. Phys.* 51 (5), 351–365. doi:10.1016/0021-9169(89)90117-7
- Pinto, O., Gonzalez, W. D., and Gonzalez, A. (1989). Time variations of X Ray fluxes at the South Atlantic Magnetic Anomaly in association with a strong geomagnetic storm. *J. Geophys. Res.* 94, 17275–17280. doi:10.1029/ja094ia12p17275
- Ponomarev, E. A., Sedykh, P. A., and Urbanovich, V. D. (2006). Bow shock as a power source for magnetospheric processes. *J. Atmos. Solar-Terrestrial Phys.* 68 (6), 685–690. doi:10.1016/j.jastp.2005.11.007
- Rees, M. H. (1963). Auroral ionization and excitation by incident energetic electrons. *Planet. Space Sci.* 11 (10), 1209–1218. doi:10.1016/0032-0633(63)90252-6
- Reinisch, B. W., Galkin, I. A., Khmyrov, G. M., Kozlov, A. V., Bibl, K., Lisysyan, I. A., et al. (2009). New Digisonde for research and monitoring applications. *Radio Sci.* 44 (1), RS0A24. doi:10.1029/2008rs004115
- Reinisch, B. W., Haines, D. M., Bibl, K., Galkin, I., Huang, X., Kitrosser, D. F., et al. (1997). Ionospheric sounding in support of over-the-horizon radar. *Radio Sci.* 32 (4), 1681–1694. doi:10.1029/97rs00841
- Resende, L. C. A., Batista, I. S., Denardini, C. M., Batista, P. P., Carrasco, A. J., Andrioli, V. F., et al. (2017). Simulations of blanketing sporadic E-layer over the Brazilian sector driven by tidal winds. *J. Atmos. Solar-Terrestrial Phys.* 154, 104–114. doi:10.1016/j.jastp.2016.12.012
- Resende, L. C. A., Denardini, C. M., and Batista, I. S. (2013). Abnormal fb Es enhancements in equatorial Es layers during magnetic storms of solar cycle 23. *J. Atmos. Solar-Terrestrial Phys.* 102, 228–234. doi:10.1016/j.jastp.2013.05.020
- Richardson, I. G., and Cane, H. V. (2010). Near-earth interplanetary coronal mass ejections during solar cycle 23 (1996 - 2009): Catalog and summary of properties. *Sol. Phys.* 264 (1), 189–237. doi:10.1007/s11207-010-9568-6
- Richardson, I. G., and Cane, H. V. (2012). Solar wind drivers of geomagnetic storms during more than four solar cycles. *J. Space Weather Space Clim.* 2, A01. doi:10.1051/swsc/2012001
- Rodger, C. J., Kavanagh, A. J., Clilverd, M. A., and Marple, S. R. (2013). Comparison between POES energetic electron precipitation observations and riometer absorptions: Implications for determining true precipitation fluxes. *J. Geophys. Res. Space Phys.* 118 (12), 7810–7821. doi:10.1002/2013JA019439
- Roederer, J. G. (1967). On the adiabatic motion of energetic particles in a model magnetosphere. *J. Geophys. Res.* 72 (3), 981–992. doi:10.1029/jz072i003p00981

- Russell, C. T., Holzer, R. E., and Smith, E. J. (1969). OGO 3 observations of ELF noise in the magnetosphere: 1. Spatial extent and frequency of occurrence. *J. Geophys. Res.* 74 (3), 755–777. doi:10.1029/ja074i003p00755
- Santolík, O., Parrot, M., and Lefeuvre, F. (2003). Singular value decomposition methods for wave propagation analysis. *Radio Sci.* 38 (1), 1010. doi:10.1029/2000RS002523
- Santolík, O., Pickett, J. S., Gurnett, D. A., Maksimovic, M., and Cornilleau-Wehrin, N. (2002). Spatiotemporal variability and propagation of equatorial noise observed by Cluster. *J. Geophys. Res.* 107, SMP 43-51–SMP 43-48. doi:10.1029/2001JA009159
- Santos, A. M., Abdu, M. A., Souza, J. R., Sobral, J. H. A., Batista, I. S., and Denardini, C. M. (2016). Storm time equatorial plasma bubble zonal drift reversal due to disturbance Hall electric field over the Brazilian region. *J. Geophys. Res. Space Phys.* 121, 5594–5612. doi:10.1002/2015JA022179
- Shklyar, D., and Matsumoto, H. (2009). Oblique whistler-mode waves in the inhomogeneous magnetospheric plasma: Resonant interactions with energetic charged particles. *Surv. Geophys.* 30, 55–104. doi:10.1007/s10712-009-9061-7
- Stone, E. C., Frandsen, A. M., Mewaldt, R. A., Christian, E. R., Margolies, D., Ormes, J. F., et al. (1998). The advanced composition explorer. *Space Sci. Rev.* 86 (1/4), 1–22. doi:10.1023/A:1005082526237
- Thomas, N., Shiokawa, K., Miyoshi, Y., Kasahara, Y., Shinohara, I., Kumamoto, A., et al. (2021). Investigation of small scale electron density irregularities observed by the Arase and Van Allen Probes satellites inside and outside the plasmasphere. *JGR. Space Phys.* 126, e2020JA027917. doi:10.1029/2020JA027917
- Tsurutani, B. T., Smith, E. J., and Thorne, R. M. (1975). Electromagnetic hiss and relativistic electron losses in the inner zone. *J. Geophys. Res.* 80, 600–607. doi:10.1029/ja080i004p00600
- Watt, C. E. J., Allison, H. J., Meredith, N. P., Thompson, R. L., Bentley, S. N., Rae, I. J., et al. (2019). Variability of quasilinear diffusion coefficients for plasmaspheric hiss. *J. Geophys. Res. Space Phys.* 124, 8488–8506. doi:10.1029/2018JA026401
- Whalen, J. A., Buchau, J., and Wagner, R. A. (1971). Airborne ionospheric and optical measurements of noontime aurora. *J. Atmos. Terr. Phys.* 33 (4), 661–678. doi:10.1016/0021-9169(71)90066-3
- Whitehead, J. D. (1970). Production and prediction of sporadic E. *Rev. Geophys.* 8 (1), 65. doi:10.1029/RG008i001p00065
- Wygant, J. R., Bonnell, J. W., Goetz, K., Ergun, R. E., Mozer, F. S., Bale, S. D., et al. (2013). The electric field and waves instruments on the radiation belt storm probes mission. *Space Sci. Rev.* 179 (1–4), 183–220. doi:10.1007/s11214-013-0013-7
- Xiao, F., Yang, C., Su, Z., Zhou, Q., He, Z., He, Y., et al. (2015). Wave-driven butterfly distribution of Van Allen belt relativistic electrons. *Nat. Commun.* 6 (1), 8590. doi:10.1038/ncomms9590
- Yahnin, A. G., Titova, E. E., Demekhov, A. G., Yahnina, T. A., Popova, T. A., Lyubchich, A., et al. (2019). Simultaneous observations of EMIC waves, ELF/VLF waves, and energetic particle precipitation during multiple compressions of the magnetosphere. *Geomagn. Aeron.* 59, 668–680. doi:10.1134/S0016793219060148
- Yu, B., Scott, C. J., Xue, X., Yue, X., and Dou, X. (2020). Derivation of global ionospheric Sporadic E critical frequency (f_oE_s) data from the amplitude variations in GPS/GNSS radio occultations. *R. Soc. Open Sci.* 7, 200320. doi:10.1098/rsos.200320
- Zhelavskaya, I. S., Spasojevic, M., Shprits, Y. Y., and Kurth, W. S. (2016). Automated determination of electron density from electric field measurements on the Van Allen Probes spacecraft: field measurements on the Van Allen Probes spacecraft. *JGR. Space Phys.* 121, 4611–4625. doi:10.1002/2015JA022132